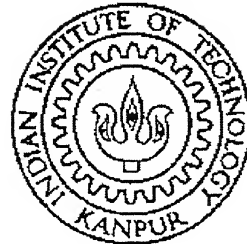


**ROLE OF THERMAL GRADIENTS IN  
BLANKET DEPOSITION OF TUNGSTEN IN  
INTERCONNECT TRENCHES**

**By**

**Prabhanjan Mishra**



**DEPARTMENT OF MATERIALS AND METALLURGICAL ENGINEERING  
INDIAN INSTITUTE OF TECHNOLOGY, KANPUR**

**November, 1999**

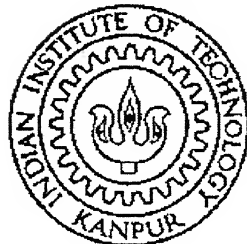
# **Role of Thermal Gradients in Blanket Deposition of Tungsten in interconnect trenches**

*A Thesis Submitted  
in partial Fulfillment of the Requirements  
for the degree of*

**Master of Technology**

**By**

**Prabhanjan Mishra**



to the

**DEPARTMENT OF MATERIALS AND METALLURGICAL ENGINEERING  
INDIAN INSTITUTE OF TECHNOLOGY, KANPUR**

**November, 1999**

2 MAR 2000 /MME  
CENTRAL LIBRARY  
I.I.T., KANPUR

Call No. A 130444

TH

MME/1999/m

M 6872



A130444

**Dedicated**

**to**

**My Parents**



## CERTIFICATE

It is certified that the work contained in the thesis entitled ***Role of Thermal Gradients in Blanket Deposition of Tungsten in Interconnect Trenches*** by **Prabhanjan Mishra** has been carried out under my supervision and this work has not been submitted elsewhere for a degree.

Dr. Deepak Gupta

Asst. Professor,

Dept. of Materials and Metallurgical Engg.,

Indian Institute of Technology,

Kanpur-208016

## **TABLE OF CONTENTS**

<b>Abstract</b> .....	iii
<b>Acknowledgements</b> .....	v
<b>List of Figures</b> .....	vi
<b>Chapter 1: INTRODUCTION</b> .....	01
1.1 Background .....	01
1.2 Literature Review .....	04
1.3 Objectives of the present study .....	10
<b>Chapter 2: CHEMICAL VAPOUR DEPOSITION: A TWO DIMENSIONAL MODEL</b> .....	12
2.1 The model .....	12
2.2 Method of discretizaion and solution procedure .....	17
2.3 Growth and boundary movement .....	19
<b>List of Symbols Used in Chapter 2</b> .....	23
<b>Appendix I</b> .....	24
<b>Appendix II</b> .....	26
<b>Appendix III</b> .....	27
<b>Chapter 3: RESULTS AND DISCUSSION</b> .....	34
3.1 Deposition under 773 K .....	37
3.2 Deposition under 673 K .....	43
3.3 Deposition under 573 K .....	52
3.4 The Thermal Gradient .....	61
<b>Chapter 4: CONCLUSION</b> .....	63
<b>References</b> .....	65

## ABSTRACT

Blanket chemical vapour deposited tungsten (W-CVD) is routinely employed to fabricate reliable contacts for sub-micron multilevel metallization. The deposition is achieved by hydrogen reduction of tungsten hexafluoride. In case of a trench, as an example, as the aspect ratio, defined as the ratio of depth to width of a trench, increases, a void may form, leading to serious problems in the reliability of integrated circuits (ICs).

In the present work we investigate a novel idea of imposing a controlled thermal gradient along the vertical direction of the trench, in a manner that the base of the trench is hotter than its mouth.

In the mass transport and chemical reaction model presented here, Knudsen flow, viscous flow and ordinary diffusion are all taken into account. The mass flux in the two-dimensional model is expressed according to the “dusty gas” model. The model equations are numerically solved via a finite difference discretized approach for the parameters corresponding to tungsten deposition by hydrogen reduction of tungsten hexafluoride. It also accounts for the changes in the trench shape that occur during the deposition of tungsten on the trench boundaries.

The isothermal deposition profile computed for trench of different aspect ratios show the formation of a void at deposition temperatures 673 and 773 K. In order to attain void free deposition, a linear temperature gradient is imposed keeping the temperature at mouth of the trenches at 673 and 773 K, respectively. At the most the base of the trench is 3 K hotter. We find excellent step coverage for different aspect ratios in the range 2-5 (ratio of trench depth to width of the trench), at deposition temperatures of 673 K. Even

after an application of thermal gradient, void still forms at 773 K, while at 573 K, also investigated in this work, no void forms even under isothermal process.

We also discuss the dielectric material that could support the thermal gradient applied in this work. We suggest that either commonly used SiO<sub>2</sub> layer will have to be processed differently, or new material will be used to account for required value of thermal conductivity. In this regard, polyamide or fluoropolyamide dielectrics may be more suited, which are also candidates for interlayer dielectric for their dielectric properties.

**Keywords:** CVD; contacts; step coverage; ICs

## **ACKNOWLEDGEMENTS**

I would like to express my deep sense of gratitude to Dr. Deepak Gupta for his invaluable guidance throughout my M.Tech programme. It is because of his constant encouragement and motivation, I could accomplish some fruitful results in my thesis work. I am always grateful to him for sparing his precious time and providing valuable suggestions at each point.

I would like to pay my sincere regards to Dr. M. Katiyar and Dr. B. Deo for providing motivation and encouragement during the thesis work.

I am thankful to all my friends and classmates, especially Balaji, Murali, Tanmay, Girija, Kaushik and Pavitda for giving me a good company and making my stay, at IIT Kanpur, a pleasant and memorable one.

**Prabhanjan Mishra**

## LIST OF FIGURES

### **Chapter 1**

Fig.1: Schematic of a void formation in blanket W CVD.....11

### **Chapter 2**

Fig.1: Schematic of a trench that is to be filled with W.....13

Fig.2: The computational domain.....14

Fig.3: Schematic showing boundary conditions.....17

Fig.4: Discretization at a node point.....18

Fig.5: Points a, b and c on the mesh, equally spaced in X-direction and logarithmically along Y-direction.....20

Fig.6: Depiction of boundary movement along X-direction.....21

### **Chapter 3**

Fig.1: Isothermal deposition profile at 773 K for  $W_0=0.35\mu\text{m}$  and mesh size 101x101.....36

Fig.2: Schematic of a trench corresponding to Fig.1.....37

Fig.3: Isothermal deposition profile at 773 K for  $W_0=0.35\mu\text{m}$  and mesh size 51x51.....38

Fig.4: Isothermal deposition profile at 773 K for  $W_0=0.5\mu\text{m}$ .....39

Fig.5: Isothermal deposition profile at 773 K for  $W_0=0.25\mu\text{m}$ .....40

Fig.6: Isothermal deposition profile at 773 K for  $W_0=0.2\mu\text{m}$ .....41

Fig.7: Modified deposition profile of Fig.4 under non-isothermal condition.....43

Fig.8: Modified deposition profile of Fig.3 under non-isothermal condition.....44

Fig.9: Modified deposition profile of Fig.5 under non-isothermal condition.....	45
Fig.10: Modified deposition profile of Fig.6 under non-isothermal condition.....	46
Fig.11: Isothermal deposition profile at 673 K for $W_0=0.5\mu\text{m}$ .....	47
Fig.12: Isothermal deposition profile at 673 K for $W_0=0.35\mu\text{m}$ .....	48
Fig.13: Isothermal deposition profile at 673 K for $W_0=0.25\mu\text{m}$ .....	49
Fig.14: Isothermal deposition profile at 673 K for $W_0=0.2\mu\text{m}$ .....	50
Fig.15: Modified deposition profile of Fig.11 after application of $\Delta T=1\text{ K}$ .....	52
Fig.16: Modified deposition profile of Fig.12 after application of $\Delta T=2\text{ K}$ .....	53
Fig.17: Modified deposition profile of Fig.13 after application of $\Delta T=3\text{ K}$ .....	54
Fig.18: Modified deposition profile of Fig.14 after application of $\Delta T=3\text{ K}$ .....	55
Fig.19: Isothermal deposition profile at 573 K for $W_0=0.5\mu\text{m}$ .....	57
Fig.20: Isothermal deposition profile at 573 K for $W_0=0.35\mu\text{m}$ .....	58
Fig.21: Isothermal deposition profile at 573 K for $W_0=0.25\mu\text{m}$ .....	59
Fig.22: Isothermal deposition profile at 573 K for $W_0=0.2\mu\text{m}$ .....	60

## CHAPTER 1

### INTRODUCTION

#### **1.1 BACKGROUND**

The formation and behavior of metal-semiconductor contacts play a vital role in the very large scale integrated (VLSI) technology. For metal oxide semiconductor (MOS) transistors, metals and their silicides are used as gate electrodes, contacts, diffusion barriers and in interconnect metallization.

With advances in integrated circuit technology, device dimensions are being scaled down to submicron levels. Also the integrated circuits (ICs) require chips having fast switching speed, high reliability and low cost per function. The larger size and high complexity chips require closely placed long interconnect lines with a small area of cross section. As a result, the resistance-capacitance (RC) time delay becomes significant. The RC time constant of a interconnect is given by:

$$RC = R_s L^2 \epsilon / t$$

where  $R_s$  and  $L$  are the sheet resistance and length of the connection, respectively;  $t$  and  $\epsilon$  are the thickness and dielectric constant of the insulating film, respectively. Thus the performance of a large circuit will be seriously affected by the interconnections present in it. In order to achieve higher switching speed the sheet resistance ( $R_s$ ) of the interconnect should be reduced.

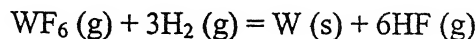
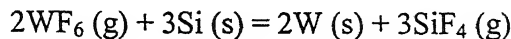
Heavily doped polycrystalline silicon (poly-Si), aluminum (Al), and aluminum alloys have been widely used in VLSI circuits. However, the high electrical resistivity value ( $\rho = 500 \mu\text{ohm.cm}$ ) of poly-Si results in considerable signal propagation delay and joule heating. This limits its suitability for metallization of submicron size devices. In the case of Al, in- spite of its low electrical resistivity ( $\rho = 2.7 \mu\text{ohm-cm}$ ), it also has two major drawbacks which limits its use in ICs. First, at high current density, electromigration destroys the physical integrity of aluminum interconnect lines. Second, Si has a tendency to diffuse into aluminum grain boundaries, resulting in spikes of aluminum. These Al spikes cause leakage and possible shorting of the junctions[1].

Another severe limitation of using Al is its nonconformal coverage over the interconnects. Because of the inherent conformal coverage properties of chemical vapour deposition (CVD), tungsten deposited by CVD is a candidate process in interconnects having high aspect ratios. The following features of tungsten (W) make it attractive for VLSI circuits.

- Deposition can be selective or non-selective.
- It is easy to pattern non-selective tungsten films by wet or dry etching techniques.
- Excellent conformal coverage is shown by non-selective or blanket depositions process.
- Films can be deposited in hot wall or cold wall CVD reactors, over a wide range of temperatures.
- Excellent electromigration resistance of W films compared to Al.
- Good compromise between prevention of junction spiking and an increased electrical resistivity (compared to Al).

- The thermal expansion coefficients of tungsten and silicon are similar, which reduces the stress at the interface.

Tungsten hexafluoride ( $\text{WF}_6$ ) is a suitable precursor gas for tungsten deposition in ICs. CVD of tungsten can be achieved both by silicon reduction and hydrogen reduction of  $\text{WF}_6$ , according to the following reactions:



According to the free energy data, silicon reduction of  $\text{WF}_6$  is thermodynamically favourable over the hydrogen reduction reaction. However, the silicon reduction reaction is self-limiting, that is, after a film of about  $100\text{-}200\text{ \AA}$ , the reaction stops. Subsequently, thicker tungsten films can be grown on silicon substrates by  $\text{H}_2$  reduction of  $\text{WF}_6$ . There is no inherent limit on the thickness of tungsten films that can be deposited by  $\text{H}_2$  reduction reaction.

Tungsten deposition in the interconnects of ICs can be achieved selectively or non-selectively. The non-selective deposition is often termed as blanket deposition. In blanket tungsten deposition, after metal deposition of W by silicon reduction reaction, tungsten is deposited non-selectively on the already deposited metal in the trench as well as on the dielectric by hydrogen reduction reaction. The excess tungsten deposited on the plug and the other areas is etched off thereafter. On the other hand, in case of selective deposition, tungsten is deposited only in the trench and not on the dielectric or other insulators. This selective deposition could be used to eliminate mask and etch steps, required in the case of blanket deposition, to remove excess metal. Here tungsten deposition first proceeds by silicon reduction and subsequent W deposition occurs on the

already grown tungsten by hydrogen reduction. However, this process requires specific processing conditions and a tight control of process variables. Moreover, the selective nature of tungsten deposition often breaks down before the deposition is complete.

Thus frequent loss of selectivity makes the selective tungsten deposition process less popular in commercial reactors and, the blanket tungsten deposition is the preferred approach.

## 1.2 LITERATURE REVIEW

In the following, a review of literature is provided on tungsten CVD for filling interconnects in VLSI circuits, concentrating especially on a void that is formed inside the trench while depositing tungsten from its precursor gas  $WF_6$ .

In an integrated tungsten deposition and etchback plug fabrication process, in a cold wall single wafer CVD chamber[2], at a temperature above  $300^0C$ , it is possible to obtain uniform tungsten plugs in devices without degrading the electrical performances of the contacts (compared to standard aluminum case).

Tungsten deposition is usually carried out by CVD process, which in comparison to PVD, yields a better step coverage. The deposition of tungsten starts by reduction of  $WF_6$  with silicon substrate. But due to the self-limiting nature of this reaction, subsequent tungsten deposition is carried out by  $H_2$  reduction.

Tungsten deposition can be done in two ways: blanket and selective. A review of the current W plug process is provided by Ireland[3], who discusses the role of dopants in

obtaining good metal/silicon interface, the associated cleans, barrier layers and then tungsten deposition and etch back processes.

The selective deposition has received much attention in the past. But due to the tight process conditions[4], reactor design and selectivity, this process has not been fully commercialized yet. On the other hand, blanket deposition which suffers from the drawbacks of incomplete filling, is still practised in majority of VLSI fabrication processes.

Pauleau and Lami[5] investigated the kinetics and mechanism of W deposition both by silicon and hydrogen reduction. Under silicon reduction it was found that[5,6], the deposition is purely selective and no encroachment of W film occurs along Si/SiO<sub>2</sub> interface. It was also found that within a temperature range of 300-475°C; the film thickness is limited between 100 and 150 Å<sup>0</sup>, indicating self-limiting nature of silicon reduction. Another related work is proceeded by Yeh et al.[7], in which they were able to deposit selective W film by silane reduction of tungsten hexafluoride. The selectivity becomes excellent at a deposition temperature of 280-350°C and a flow rate of SiH<sub>4</sub>/WF<sub>6</sub>, less than 0.6. However, at temperatures above 350°C, W starts nucleating on SiO<sub>2</sub> surface, because of the by-product SiF<sub>2</sub> with WF<sub>6</sub>, leading to selectivity loss. In WF<sub>6</sub>-H<sub>2</sub> deposition, the rate limiting mechanism was found to be dissociation of hydrogen on substrate and the reaction is one-half order in H<sub>2</sub> concentration and zero order in WF<sub>6</sub> concentration[8]. But this rate expression does not account for the fact that rate must go to zero as the concentration of WF<sub>6</sub> goes to zero. Therefore, Jain et al.[9] modified the rate expression as:

$$\text{Rate} = 0.00827 \exp\left(-\frac{8800}{T}\right) P_H^{0.5} \left[ \frac{P_{WF_6} (1 + k_f P_{WF_6}^0)}{P_{WF_6}^0 (1 + k_f P_{WF_6})} \right] \text{mol/cm}^2/\text{s} \quad (1)$$

where  $T$  is the temperature in K,  $P_H$  and  $P_{WF_6}$  are the hydrogen and tungsten hexafluoride partial pressures in Torr, respectively,  $P_{WF_6}^0$  is the partial pressure of tungsten hexafluoride at the top of the wafer and  $k_f$  is a constant whose value is  $1000 \text{ Torr}^{-1}$ .

A low temperature ( $250\text{-}500^\circ\text{C}$ ) is required for selective deposition of W by  $H_2$  reduction. Moreover, the concentration of both  $H_2$  and  $WF_6$  must be low, that is, deposition rate must be slow. But in this case the selectivity is maintained only for a short deposition time (15-30min). Many investigations tried to find out the reason for loss of selectivity. Pauleau and Lami[5] associate loss of selectivity to presence of high concentration of by-product gas HF, whose interaction with  $SiO_2$  results in nucleation of W on oxide. Broadbent and Stacy[6] finds that the loss of selectivity is mainly due to presence of silicon containing by products, such as  $SiF_4$ . The reason for loss of selectivity is also explained by Kuijlaars et al.[10] and Werner et al.[11]. Experimental evidence reveals that nucleation of tungsten occurs in the areas farther from the trench, which means the loss of selectivity is primarily due to gas phase diffusion rather than surface diffusion. The nucleation accelerates by the presence of additional W surfaces in the reactor[11].

Here it will be useful to cite two theories that explain the loss of selectivity. In the first, HF is thought to be responsible, which reacts with  $SiO_2$  to form  $SiF_x$  ( $x < 3$ ) over a tungsten catalyst. This is followed by the interaction of reactive  $SiF_x$  with  $WF_6$  to form a deficient  $WF_y$ , which when adsorbed on oxide surface form tungsten islands. However, experiments do not match well with the degree of selectivity loss. Another theory, which

deals with observation of adsorbed species on oxide, suggests presence of sub-fluorides  $\text{WF}_5$ [12].

Apart from the experimental studies, some modeling of tungsten CVD is also reviewed. Ulacia et al.[13] studied the physical and chemical simulation of a tungsten CVD reactor using fluid dynamics equations. The effect of thermal diffusion has been completely neglected. This study provides a better understanding of the CVD process, optimizing the variables that affect deposition rate and film uniformity. A similar work is carried out by Cale et al.[14], where they have decreased the processing time for a given step coverage by varying the deposition rate in a prescribed manner during the process. A theoretical model by Joshi et al.[15] illustrates that the growth rate depends on the trench size, aspect ratio and  $\text{WF}_6$  concentration.

In another work, Kuijlaars et al.[16] developed a model to study the influence of process condition and the concentration distribution of tungsten sub-fluorides, which are believed to be the reasons for loss of selectivity. They found that low temperature, low pressure and large total gas flow rate enhances selective deposition. However, their study left some unresolved problem regarding the chemistry of the species, to which some ad hoc modifications were made.

From several modeling and experimental studies on selective W deposition, it is obvious that tight process control is needed for enhancing selectivity e.g.

- Low pressure followed by low growth rates.
- Low temperature.
- Cooled reactor wall to minimize reaction and hence product gases.
- Coating the back of the wafer for avoiding W island formation.

- Increased flow rates to minimize resident time and product gases.

Furthermore, low growth rate implies longer processing time, which again causes loss of selectivity. Therefore although selective tungsten deposition is desirable because it avoids the additional step of etch back, it is still not the choice for manufacturability.

From the discussion above, it is clear that still blanket W deposition processes has to be used for depositing W in trenches of ICs. This allows much more relaxed control and also the throughput is large. However, the blanket tungsten deposition suffers from a problem of void formation[17], which may affect the reliability of interconnects in ICs.

The experimental work of Chen et al.[18] illustrates the deposition of blanket tungsten layer followed by etch back. Depositions are performed on both patterned and unpatterned wafers to study the plug formation and to characterize the film properties. Excellent step coverage is reported for gas ratio 1:2 of  $\text{SiH}_4$  to  $\text{WF}_6$ . The etch back is done by  $\text{SF}_6$  and  $\text{N}_2$ .

Apart from experimental studies, literature provides many models for filling a trench during blanket deposition. Jain et al.[9] provide a comparison of a diffusion reaction model and a ballistic transport reaction model and find a particle based line of sight model to give better predictions. However, this approach is limited to regimes where assumption of Knudsen flow is valid.

Hasper et al.[19] presented a model to calculate the step coverage of blanket tungsten low-pressure chemical vapour deposition (LPCVD) by hydrogen reduction as well as silicon reduction. For hydrogen reduction, a good agreement between experimental and model step coverage is obtained. HF is found to have no influence on step coverage. The step coverage, in high aspect ratio ( $2\mu\text{m} \times 10\mu\text{m}$ ) trenches is

enhanced by high  $\text{WF}_6$  concentration and low growth rate. They obtained a step coverage of 95% in trenches with aspect ratio 5 uniformly over a 6 inch wafer. Schmitz and Hasper[17] also studied the step coverage of blanket W CVD for aspect ratios 0.5, 1.0 and 2.0. The flow rate of  $\text{WF}_6$  is 20 sccm., and that of  $\text{H}_2$  is 500 sccm., at a temperature of  $430^{\circ}\text{C}$ . They found that the size of void increases with increase in aspect ratio of the trench. The results are also experimentally verified. Egashira et al.[20] also presented a model on blanket CVD of tungsten. Here they have described the reaction mechanism of  $\text{WSi}_x$  blanket CVD by  $\text{WF}_6/\text{Si}_2\text{H}_6$ . They have also predicted the reactor performance based on the data of a tubular reactor. The simulation is aimed at the optimization of a newly developed reactor.

Another model by Klejin et al.[21] studies the influence of  $\text{WF}_6$  concentration on growth rate in W LPCVD by hydrogen reduction, both experimentally and mathematically. Model predictions are in good agreement with experimental growth rates. Above a certain critical partial pressure of  $\text{WF}_6$ , growth rate is found to be independent of partial pressure of  $\text{WF}_6$ . Thermal diffusion in cold wall reactor is found to be very important.

Most models reported in literature are two-dimensional. A two dimensional model is sufficient to provide insight into reasons for void formation. However, a three-dimensional model is presented by Bar and Lorenz[22], which is more realistic and it can be applicable to arbitrary shapes.

Yun and Park[4] studied the numerical solution for high aspect ratio trench models to study the step coverage in LPCVD process. They use Monte Carlo simulation and string algorithm. Sticking coefficient, surface diffusion coefficient, direct deposition

and various re-emission mechanisms are included in this model. It is found that the step coverage becomes poor as the temperature and aspect ratio increases. Experimental results do agree with simulated ones. Finally, they concluded that low temperature operation below 280  $^{\circ}\text{C}$  is proposed as a way to deposit the conformal tungsten film with good step coverage.

In another Monte Carlo simulation model for W LPCVD on silicon substrate by hydrogen reduction, Kim et al.[23] showed the non-linear dependence of  $\text{WF}_6$  concentration on growth rate. The study adopts a simple-surface reaction model assuming adsorption of  $\text{WF}_6$  only on trench walls. They showed that growth rates increase linearly.

From this review, it is clear that blanket W deposition is more manufacturable than selective W deposition. Machines are now available, in which both deposition and subsequent etch back process can be integrated. But, both experimental and model studies demonstrate the formation of a void during the filling process of the trench. The void formation becomes more pronounced as the deposition temperature and aspect ratio of the trench increases, which is eventually a reliability issue.

### 1.3 OBJECTIVES OF THE PRESENT STUDY

A silicon wafer contains a number of devices, electrically connected by interconnections. These multiple layers of interconnects are connected by tungsten plugs. The shapes of these plugs are, for example, rectangular trenches having width less than a  $\mu\text{m}$  and length of a few  $\mu\text{m}$ . For making contacts of tungsten in these trenches,  $\text{WF}_6$  is passed over the wafer along with hydrogen. These gases diffuse into the trench, where

they react at the walls of the trench. As a result tungsten is deposited on the walls and HF diffuses out. Because these source gases have to diffuse throughout the depth of the trench, concentration gradient may develop, with higher concentration at the feature mouth. Since the concentration of the reacting source gases is more at the mouth, the reaction rate is also faster there than at the bottom of the trench, that is, the rate of growth of tungsten layer is more at the mouth. This leads to the closure of the mouth before complete filling of the trench, resulting in formation of a void in the trench. This feature can adversely affect device reliability and device performance. Schematically, this situation is shown in Fig.1.

The objective of the present work is to ensure voidless deposition of tungsten in the rectangular trenches of the interconnects of ICs. Optimizing process parameters that give the best step coverage can do this. In other words, we have to proceed with deposition in kinetic control regime, where concentration gradients are minimized. This is the reason why we get better step coverage at low temperature. But at low temperature the deposition time is very large, which affects the throughput.

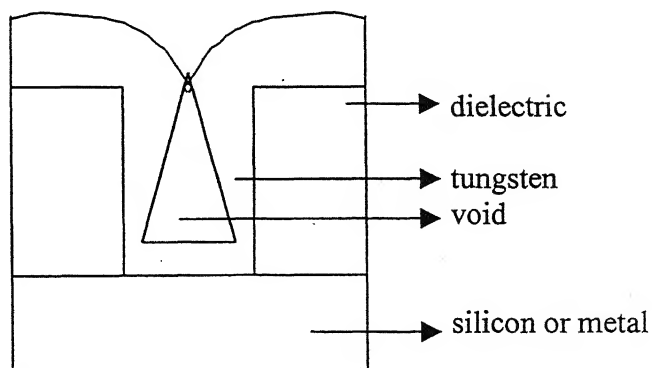


Fig.1: Schematic of a void formation in blanket W CVD.

Obviously, it will be much better if W CVD can be carried out at higher temperature and (atmospheric) pressure without void formation. Thus the goal of this work is to explore new ways in which this can be accomplished. One way would be to impose a temperature gradient along the vertical direction of the trench, so that, its bottom will be hotter than the mouth. As a result, W will preferentially deposit at the base of the mouth and the trench would fill inside-out.

## CHAPTER 2

### CHEMICAL VAPOUR DEPOSITION : A TWO DIMENSIONAL MODEL

#### 2.1 THE MODEL

As discussed in the preceding chapter the process of filling trenches of tungsten in interconnects of ICs is performed by chemical vapour deposition (CVD) process. This chapter deals with two-dimensional modeling of a trench filling process by CVD.

In VLSI device fabrication process, each device contains submicron trenches/vias. The shape of these features is taken as a rectangular section. A cross section of the trench, infinitely long in the third dimension is shown in Fig.1.

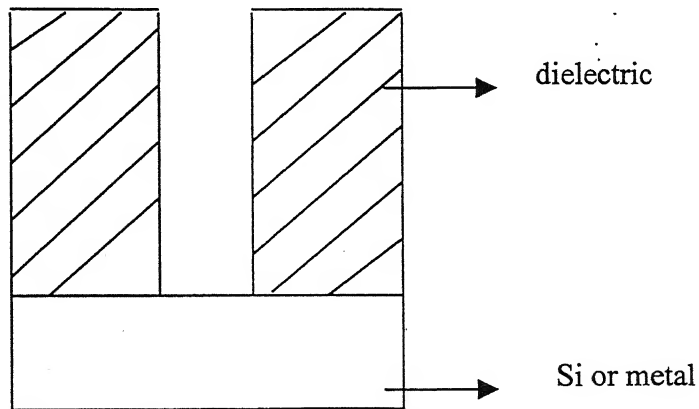


Fig.1: Schematic of a cross-section of a trench

We consider only one half of the trench as the computational domain for mass transport calculations, allowing for symmetry about  $x=0$  (see Fig.2). The initial length and half-width of the trench is taken as  $L_0$  and  $W_0$ , respectively.

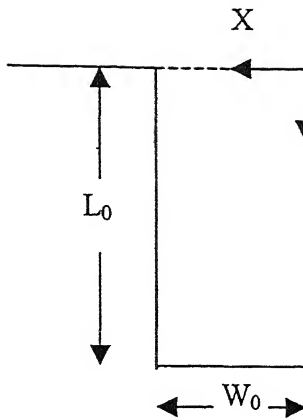
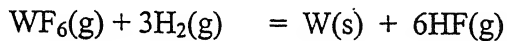


Fig.2: The computational domain

Deposition of tungsten by CVD using  $\text{WF}_6$  as the source gas proceeds according to the following heterogeneous chemical reaction:



The product gas HF diffuses out of the trench. The rate of tungsten deposition by  $\text{H}_2$  reduction of  $\text{WF}_6$  has been reported as[9]:

$$R = 2.2649 \times 10^{-4} \exp \left( \frac{-8800}{T} \right) P^{0.5} X_{\text{H}_2}^{0.5} \left[ \frac{P_{\text{WF}_6}^0 (1 + k_f P_{\text{WF}_6}^0)}{P_{\text{WF}_6}^0 (1 + k_f P_{\text{WF}_6}^0)} \right] \quad (1)$$

where  $k_f = 0.75006 \text{ (dyne/cm}^2\text{)}^{-1}$ ,  $P_{\text{WF}_6}^0$  is the partial pressure of  $\text{WF}_6$  at the mouth of the via. For any significant value of  $P_{\text{WF}_6}^0$ , the term in the square bracket in equation (1) goes to unity.

An expression for molar flux is determined from 'dusty' gas model[27]. This model takes into account ordinary diffusion, viscous flow and Knudsen flow and has been successfully applied before[28]. The derivation of flux expression starts from kinetic theory of gases. Here the multicomponent diffusion of gases occurs by binary collision between gas molecules. The solid in this model is also considered a heavy,

immobile gas. Knudsen diffusion is included assuming binary collision between gas molecules and the dust gas. Furthermore, viscous flow is also considered.

Neglecting thermal diffusion, the flux expression can be written as follows:

$$\frac{1}{c} \sum \frac{1}{\vartheta_{ij}} \left[ X_j \bar{N}_i - X_i \bar{N}_j \right] + \frac{\bar{N}_i}{c D_{ik}} = - \nabla X_i - X_i \left[ \frac{1}{P} + \frac{W^2}{3\eta D_{ik}} \right] \nabla P \quad (2)$$

for  $i, j = 1, 2, 3$

Subscripts 1,2,3 indicate  $H_2$ ,  $WF_6$  and  $HF$  respectively. The quantities  $D_{ik}$ ,  $\vartheta_{ij}$  and  $\eta$  are estimated by the formulae given in Appendix I. In writing this equation, we have used the fact that for a flow through a region between two parallel plates, the average velocity in direction of pressure gradient is:

$$\bar{V}_{avg.} = - \frac{W^2}{3\eta} \nabla P \quad (3)$$

Under assumption of quasi-steady state, the mass balance for  $H_2$  is

$$\nabla \cdot \bar{N}_1 = 0 \quad (4)$$

Also, from the stoichiometry of the tungsten deposition reaction,

$$\bar{N}_2 = \frac{1}{3} \bar{N}_1 \quad (5)$$

$$\bar{N}_3 = -2 \bar{N}_1 \quad (6)$$

In addition, we have ideal gas law

$$P = c R_g T \quad (7)$$

And finally,

$$\sum_{i=1}^3 X_i = 1 \quad (8)$$

Expanding eq. (2), we can write three equations in terms of molar fluxes of  $H_2$ , making use of eq. (5) to (8) at the same time.

For  $i = 1$ ,

$$\bar{N}_1 \left[ \left( \frac{2}{\vartheta_{13}} - \frac{1}{3\vartheta_{12}} \right) X_1 + \frac{X_2}{\vartheta_{12}} + \frac{X_3}{\vartheta_{13}} + \frac{1}{D_{1k}} \right] = -c \nabla X_1 - \frac{X_1}{R_g T} \left[ 1 + \frac{W^2 P}{3\eta D_{1k}} \right] \nabla P$$

or,  $\bar{N}_1 = \alpha_1 \nabla X_1 + \beta_1 \nabla P$  (10)

For  $i = 2$ ,

$$\bar{N}_1 \left[ \frac{X_1}{3\vartheta_{12}} + \left( \frac{2}{\vartheta_{23}} - \frac{1}{\vartheta_{12}} \right) X_2 + \frac{X_3}{3\vartheta_{23}} + \frac{1}{D_{2k}} \right] = -c \nabla X_2 - \frac{X_2}{R_g T} \left[ 1 + \frac{R^2 P}{3\eta D_{2k}} \right] \nabla P$$

or,  $\bar{N}_1 = \alpha_2 \nabla X_2 + \beta_2 \nabla P$  (11)

For  $i = 3$ ,

$$\bar{N}_1 \left[ \frac{2}{\vartheta_{13}} X_1 + \frac{2}{\vartheta_{23}} X_2 + \left( \frac{1}{\vartheta_{13}} + \frac{1}{3\vartheta_{23}} \right) X_3 + \frac{1}{D_{3k}} \right] = -c \nabla X_3 - \frac{X_3}{R_g T} \left[ 1 + \frac{R^2 P}{3\eta D_{3k}} \right] \nabla P$$

or,  $\bar{N}_1 = \alpha_3 \nabla X_1 + \alpha_3 \nabla X_2 + \beta_3 \nabla P$  (12)

where, all  $\alpha$ 's and  $\beta$ 's are listed in Appendix II.

Now, when eq. (10) to (12) are substituted in eq. (4), we get three partial differential equations containing variables  $X_1$ ,  $X_2$  and  $P$ . These are solved using the following boundary conditions.

If  $L(t)$  is the depth of the trench any time,  $t$ , and the deposition profile is as given in Fig.3, then

at,  $x=0$ ,  $\bar{N}_1 \cdot \hat{n}_1 = 0$ .

at,  $y=L(t)$ , that means, at the trench entrance

$$X_1 = X_1^0,$$

$$X_2 = X_2^0,$$

$$P = P^0.$$

and at the tungsten moving boundary,  $\bar{N}_1 \cdot \hat{n}_2 = 3\mathfrak{R}$

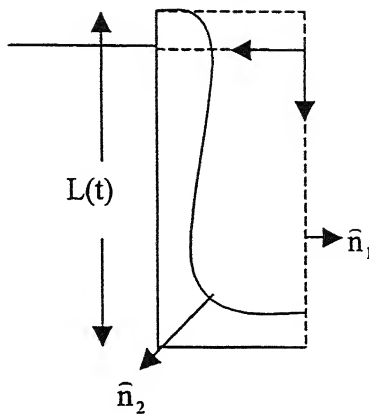


Fig.3: Schematic showing boundary conditions

## 2.2 METHOD OF DISCRETIZATION AND SOLUTION PROCEDURE

The computational domain at  $t=0$  is shown in Fig. 2. The partial differential eq. (2) is solved by a standard finite difference method. This computational domain is now discretized into a number of mesh points. Under the assumption of quasi-steady state, the finite difference form of eq. (4) at any internal point, shown in Fig. 4, in the mesh can be written as follows.

$$[\bar{N}_x^e - \bar{N}_x^w] (y_s - y_n) + [\bar{N}_y^n - \bar{N}_y^s] (x_w - x_e) = 0 \quad (15)$$

Where,  $\vec{N}_1 = N_x \hat{x} + N_y \hat{y}$  and superscripts represent the location in reference to

Fig. 4. Point N, E, S and W are points on north, east, south and west, respectively, of point P and n, e, s and w are respective mid points.

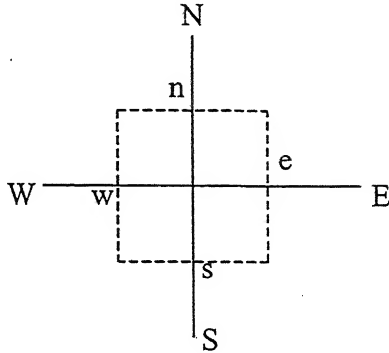


Fig.4: Discretization at a node point

There are three expressions for the flux, eq. (10)-(12), which when substituted in eq. (15) giving three finite difference equations in  $X_1$ ,  $X_2$  and  $P$  at any one node point. As an example, when eq. (10) is substituted in eq. (15), an expression for  $N_x^e$  becomes

$$N_x^e = \alpha_{1e} \left( \frac{X_{1E} - X_{1P}}{x_E - x_P} \right) + \beta_{1e} \left( \frac{P_E - P_P}{x_E - x_P} \right) \quad (16)$$

where  $x_E$  and  $x_P$  are x-locations of points E and P, respectively.  $\alpha_{1e}$  is calculated as:

$$\alpha_{1e} = \frac{\alpha_{1E} + \alpha_{1P}}{2}, \text{ in which } \alpha_{1E} \text{ and } \alpha_{1P} \text{ are values of } \alpha_1 \text{ at points E and P, respectively.}$$

In this manner, by substituting eq. (10)-(12) in eq. (15), three discretized equations are obtained. At any particular grid point of the mesh, the three discretized equations contain variables  $X_1$ ,  $X_2$  and  $P$ . The complete set of discretized equations are given in Appendix-III, which also includes boundary node points.

Clearly, the quantities  $\alpha$ 's and  $\beta$ 's used to discretize the PDE's are dependent on the variables  $X_1$ ,  $X_2$  and  $P$  themselves. So in order to compute  $\alpha$ 's and  $\beta$ 's we use a set of guessed values for  $X_1$ ,  $X_2$  and  $P$ ; then  $X_1$ ,  $X_2$  and  $P$  are computed at each node point. If the guessed values and the computed values match within  $10^{-8}$ , then convergence is achieved. Otherwise, the computed values for  $X_1$ ,  $X_2$  and  $P$  are now treated as guessed values and the procedure is repeated.

These finite difference discretized equations were solved by using the subroutines BANDEC and BANBKS[30]. These subroutines employ LU decomposition method for solving the linearised equations.

## 2.3 GROWTH AND BOUNDARY MOVEMENT

The growth rate, that is, rate of change in tungsten film thickness at any point on the wall of the via is written as:

$$\frac{dW}{dt} = \frac{M_w}{\rho_w} k P^{\frac{1}{2}} X_1^{\frac{1}{2}} \frac{P X_2}{P^0 X_2^0} \left( \frac{1+k_f P^0 X_2^0}{1+k_f P X_2} \right) \quad (17)$$

Initially,  $W = W_0$  at  $t = 0$ .

Once the concentrations ( $X_1$ ,  $X_2$  and  $P$ ) are computed at all nodes, the growth at any node point is determined according to the reaction rate in eq. (1). Thus the boundary in a direction normal to itself moves by an amount

$$dW = \frac{M_w}{\rho_w} k P^{\frac{1}{2}} X_1^{\frac{1}{2}} \frac{P X_2}{P^0 X_2^0} \left( \frac{1+k_f P^0 X_2^0}{1+k_f P X_2} \right) dt \quad (18)$$

At this stage, the growth algorithm is best discussed by considering growth at  $t=0$  during a period  $\Delta t$ ; in all subsequent time steps, the algorithm remains the same.

Consider the mesh at  $t=0$  imposed on left half of the trench, the solid lines in Fig.5, where at each node point we have already computed the concentrations. In the mesh, we have to determine the movement of the boundary points labeled "a", "b" and "c". The points "c" only move up, in  $-Y$  direction and points "b" move only in  $-X$  direction. Whereas, point "a", the left most point on the trench mouth, where boundary condition specifies concentrations  $X_1^0, X_2^0$  and  $P^0$ , moves in both  $-X$  (to  $a'$ ) and  $-Y$  (to  $a''$ ) directions.

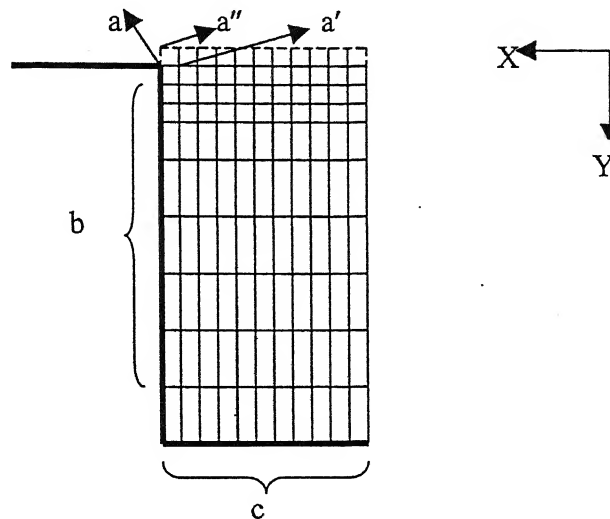


Fig.5: Point a, b and c on the mesh, equally spaced in X-direction and logarithmically in Y-direction

Since the concentrations are known at "a" a priori, the time step  $\Delta t$  is computed as time taken to move to "a''. Thus in time  $\Delta t$ , the boundary at point "a" moves to "a''. In the same duration, by an equal amount,  $W$  grows on the surface of the wafer. This fact is represented by increasing the depth of trench and adding an additional row of mesh points, seen as dotted lines in Fig. 5. These added mesh points represent the trench entrance for concentration calculations in next time step, after incrementing time by  $\Delta t$ .

Thus the point "a" also moves to point "a'", which in immediately following iteration plays the same role as "a" in this iteration.

Notice that the mesh in X direction is equally spaced. However, in the other direction, near the trench entrance, the mesh spacing increases logarithmically and then becomes equally spaced. If the mesh in Y direction were equally spaced, because  $L_0 \gg W_0$ , the mesh spacing in Y direction will be much larger than that in X direction. And because in Y direction, point "a" grows to "a'" by an amount equal to spacing in X direction (that is distance between "a" and "a'"), the vertical spacing for the newly added row will be much less than the adjacent spacing between points "a" and neighboring point "b". In order to represent the finite difference approximation accurately, we require that the mesh spacing in a direction should not increase by more than a factor of 1.2. Thus, the vertical direction spacing near the trench entrance is increased logarithmically, keeping spacing between "a" and adjacent "b" within a factor 1.2 of X direction spacing.

So far we have discussed the computation of time step and movement of point "a". Now we establish general strategy for movement of other boundary points labeled "b" and "c". Each of these points moves according to eq. (18). In time  $\Delta t$ , there is no guarantee that a point will move to another node point. For example, in Fig.6, a point "b" moves the boundary by an amount  $\Delta x$ , to a node point in between "b'" and "b'"'.

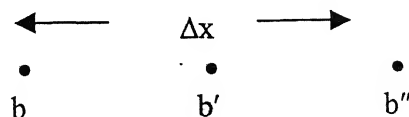


Fig.6: Depiction of boundary movement along X-direction.

However, we require that for the purpose of calculation of concentrations in the next time step, the boundary lies on a node point. This difficulty is avoided by keeping track of the actual movement of boundary at any node point, but for the purpose of calculation of concentrations, placing the boundary point on the nearest node point. Thus in the example above, while the actual displacement  $\Delta x$  is recorded and used in all subsequent calculation of boundary movement, the concentration calculations are performed by placing the boundary on the nearer of the points "b" and "b'" to determine  $\Delta x$ .

Further, growth of points labeled "c" is computed. We find that the concentration gradients in X direction are not sufficient to cause points "c" to grow by an unequal amount. Thus to simplify the problem, the growth of the lower boundary (points "c") is regarded as uniform. After the growth of the boundary to new points, these new boundary points are labeled as points "c" in the next iteration.

Once the growth of the lower boundary is computed, the nodes lying fully in W (that is other than the new boundary nodes) are rendered useless in future time steps. Also the boundary points "b" consumed due to movement of lower boundary are also removed from the reckoning; then movement of boundary at remaining "b" points is computed. According to the amount of growth, the new node points obtained as boundary are labeled as points "b" for the next iteration. We ensure that this new boundary at adjacent points "b" does not differ by one node point in X-direction; otherwise the finite difference equation in Appendix III pertinent to this boundary will not apply. In the event, this requirement is violated we start again with a finer mesh.

## List of Symbols used in Chapter 2

$c$	local gas concentration in moles per unit volume
$s_{ij}$	binary diffusion coefficient between species i and j
$D_{ik}$	Knudsen diffusion coefficient of species i
$k$	first order heterogenous rate constant
$k_B$	Boltzman constant
$k_f$	constant used in rate expression
$L_0$	initial depth of the trench
$L(t)$	depth of trench at any time t
$M_i$	molecular weight of species i
$M_W$	molecular weight of tungsten
$\bar{N}_i$	molar flux of species i
$P$	total pressure
$P_i$	partial pressure of species i
$P_i^0$	partial pressure of species i at the trench mouth
$\mathcal{R}$	rate of heterogeneous chemical reaction
$R_g$	universal gas constant
$t$	time
$T$	temperature
$\bar{V}_{avg}$	average velocity in direction of pressure gradient
$W$	local half-width of the trench at any y
$W_0$	initial half-width of the trench
$X_i$	mole fraction of species i
$\eta$	viscosity of gas mixture
$\rho_w$	density of tungsten hexafluoride

## APPENDIX I

The knudsen diffusion coefficient is given by the expression

$$D_{ik} = \frac{2}{3} W \sqrt{\frac{8R_g T}{m_i \pi}}$$

where  $m_i$  is the molecular weight gas species  $i$ .

From kinetic theory of gases the viscosity of gas species  $i$  is given as

$$\eta_i = 2.6693 \times 10^{-5} \frac{\sqrt{m_i T}}{\sigma_i^2 \Omega^{22}(T^*)}$$

where  $\eta_i$  is in  $\text{gm cm}^{-1}\text{s}^{-1}$ ,  $m_i$  is in gm,  $T$  in K and Lennard-Jones parameter  $\sigma_i$  is in  $\text{\AA}$ .  $\Omega^{22}$  is the collision integral tabulated as a function of dimensionless temperature  $T^* = k_B T / \epsilon_i$ , where  $\epsilon_i$  is another Lennard-Jones parameter.

The viscosity of gas mixture is given by Wilke's semi-empirical formula:

$$\eta = \sum_{i=1}^3 \frac{X_i \eta_i}{\sum_{j=1}^3 X_j \Phi_{ij}}$$

$$\text{where } \Phi_{ij} = \frac{\sqrt{2}}{4} \left[ 1 + \left( \frac{\eta_i}{\eta_j} \right)^{\frac{1}{2}} \left( \frac{m_j}{m_i} \right)^{\frac{1}{4}} \right]^2 \left( 1 + \frac{m_i}{m_j} \right)^{\frac{1}{2}}$$

Again from kinetic theory of gases an expression for binary diffusion coefficient is given by:

$$\Phi_{ij} = 1.8583 \times 10^{-3} \frac{\sqrt{T^3 \left( \frac{1}{m_i} + \frac{1}{m_j} \right)}}{P \sigma_{ij}^2 \Omega^{11} T_{ij}^*}$$

where  $\theta_{ij}$  is in  $\text{cm}^2/\text{s}$ ,  $T$  in  $\text{K}$ ,  $P$  in  $\text{atm}$ ,  $\sigma_{ij} = \left( \frac{\sigma_i + \sigma_j}{2} \right)$ ,  $T_{ij}^* = \frac{k_B T}{\epsilon_{ij}}$ ,

where  $\epsilon_{ij} = \sqrt{\epsilon_i \epsilon_j}$ .

## APPENDIX II

The expressions for  $\alpha$ 's and  $\beta$ 's are as follows:

$$\alpha_1 = \frac{\frac{-P}{R_g T}}{\left( \frac{2}{\vartheta_{13}} - \frac{1}{3\vartheta_{12}} \right) X_1 + \frac{X_2}{\vartheta_{12}} + \frac{X_3}{\vartheta_{13}} + \frac{1}{D_{1k}}}$$

$$\alpha_2 = \frac{\frac{-P}{R_g T}}{\frac{X_1}{3\vartheta_{12}} + \left( \frac{2}{\vartheta_{23}} - \frac{1}{\vartheta_{12}} \right) X_2 + \frac{X_3}{3\vartheta_{23}} + \frac{1}{3D_{2k}}}$$

$$\alpha_3 = \frac{\frac{-P}{R_g T}}{\frac{2X_1}{3\vartheta_{13}} + \frac{2X_2}{\vartheta_{23}} + \left( \frac{1}{\vartheta_{13}} + \frac{1}{3\vartheta_{23}} \right) X_3 + \frac{2}{D_{3k}}}$$

$$\beta_1 = \frac{-\frac{X_1}{R_g T} \left[ 1 + \frac{W^2 P}{3\eta D_{1k}} \right]}{\left( \frac{2}{\vartheta_{13}} - \frac{1}{3\vartheta_{12}} \right) X_1 + \frac{X_2}{\vartheta_{12}} + \frac{X_3}{\vartheta_{13}} + \frac{1}{D_{1k}}}$$

$$\beta_2 = \frac{-\frac{X_2}{R_g T} \left[ 1 + \frac{W^2 P}{3\eta D_{2k}} \right]}{\frac{X_1}{3\vartheta_{12}} + \left( \frac{2}{\vartheta_{23}} - \frac{1}{\vartheta_{12}} \right) X_2 + \frac{X_3}{3\vartheta_{23}} + \frac{1}{3D_{2k}}}$$

$$\beta_3 = \frac{\frac{X_3}{R_g T} \left[ 1 + \frac{W^2 P}{3\eta D_{2k}} \right]}{\frac{2X_1}{\vartheta_{13}} + \frac{2X_2}{\vartheta_{23}} + \left( \frac{1}{\vartheta_{13}} + \frac{1}{3\vartheta_{23}} \right) X_3 + \frac{2}{D_{3k}}}$$

### APPENDIX III

The expression for rate of tungsten deposition from  $\text{WF}_6$  by hydrogen reduction is given as a function of  $X_1$ ,  $X_2$  and  $P$ .

$$\mathfrak{R}(X_1, X_2, P) = k P^{0.5} X_1^{0.5} \frac{P X_2}{P^0 X_2^0} \left( \frac{1 + k_f P^0 X_2^0}{1 + k_f P X_2} \right)$$

Using multi-variable Taylor's expansion series, all the three variables can be separated.

$$\mathfrak{R}(X_1, X_2, P) = \mathfrak{R}(X_1^g, X_2^g, P^g) + (X_1 - X_1^g) \left. \frac{\partial \mathfrak{R}}{\partial X_1} \right|_g + (X_2 - X_2^g) \left. \frac{\partial \mathfrak{R}}{\partial X_2} \right|_g + (P - P^g) \left. \frac{\partial \mathfrak{R}}{\partial P} \right|_g$$

Where  $X_1^g$ ,  $X_2^g$  and  $P^g$  are the guess values at every node point.

For convenience, we can express three times of rate as:

$$3\mathfrak{R}(X_1, X_2, P) = c_0 + c_1 X_1 + c_2 X_2 + c_3 P$$

Now using this expression for  $\mathfrak{R}(X_1, X_2, P)$  we can write the discretized equations for every node of the mesh.

For a node present on 'b' of Fig.5:

Considering the fluxes only in X-direction, we can write

$$[N_x^e - \mathfrak{R}(X_1, X_2, P)](y_s - y_n) = 0$$

Using the flux expression given in equation (16), the above equation can be rewritten for all the three components.

$$1. \quad \frac{\alpha_{1e}}{(x_E - x_p)(x_p - x_e)} X_{1E} + \left[ \frac{\alpha_{1e}}{(x_E - x_p)(x_p - x_e)} + \frac{c_1}{x_p - x_e} \right] X_{1P} - \frac{c_2}{x_p - x_e} X_{2p} +$$

$$\frac{\beta_{1e}}{(x_E - x_p)(x_p - x_e)} P_E - \left[ \frac{\beta_{1e}}{(x_E - x_p)(x_p - x_e)} + \frac{c_3}{x_p - x_e} \right] P_p = \frac{c_0}{x_p - x_e}$$

$$2. \quad \frac{\alpha_{2e}}{(x_E - x_p)(x_p - x_e)} X_{1E} + \left[ \frac{\alpha_{2e}}{(x_E - x_p)(x_p - x_e)} + \frac{c_2}{x_p - x_e} \right] X_{2P} - \frac{c_1}{x_p - x_e} X_{1p} +$$

$$\frac{\beta_{2e}}{(x_E - x_p)(x_p - x_e)} P_E - \left[ \frac{\beta_{2e}}{(x_E - x_p)(x_p - x_e)} + \frac{c_3}{x_p - x_e} \right] P_p = \frac{c_0}{x_p - x_e}$$

$$3. \quad \frac{\alpha_{3e}}{(x_E - x_p)(x_p - x_e)} X_{1E} + \left[ \frac{\alpha_{3e}}{(x_E - x_p)(x_p - x_e)} + \frac{c_1}{x_p - x_e} \right] X_{1P} + \frac{\alpha_{3e}}{(x_E - x_p)(x_p - x_e)} X_{2E}$$

$$+ \left[ \frac{\alpha_{3e}}{(x_E - x_p)(x_p - x_e)} + \frac{c_2}{x_p - x_e} \right] X_{2P} + \frac{\beta_{3e}}{(x_E - x_p)(x_p - x_e)} P_E +$$

$$\left[ \frac{\beta_{3e}}{(x_E - x_p)(x_p - x_e)} + \frac{c_3}{x_p - x_e} \right] P_p = \frac{c_0}{x_p - x_e}$$

In a similar fashion, the discretized equations in other regions of the trench can be obtained.

For a node present on 'c' of Fig.5 :

$$[N_y^n - R(X_1, X_2, P)](x_w - x_e) = 0$$

$$1. \frac{\alpha_{1n}}{(y_N - y_p)(y_p - y_n)} X_{1N} - \left[ \frac{\alpha_{1n}}{(y_N - y_p)(y_p - y_n)} + \frac{c_1}{(y_p - y_n)} \right] X_{1P} - \frac{c_2}{(y_p - y_n)} X_{2P} +$$

$$\frac{\beta_{1n}}{(y_N - y_p)(y_p - y_n)} P_N - \left[ \frac{\beta_{1n}}{(y_N - y_p)(y_p - y_n)} + \frac{c_3}{(y_p - y_n)} \right] P_P = \frac{c_0}{(y_p - y_n)}$$

$$2. \frac{\alpha_{2n}}{(y_N - y_p)(y_p - y_n)} X_{2N} - \left[ \frac{\alpha_{2n}}{(y_N - y_p)(y_p - y_n)} + \frac{c_2}{(y_p - y_n)} \right] X_{2P} - \frac{c_1}{(y_p - y_n)} X_{1P} +$$

$$\frac{\beta_{2n}}{(y_N - y_p)(y_p - y_n)} P_N - \left[ \frac{\beta_{2n}}{(y_N - y_p)(y_p - y_n)} + \frac{c_3}{(y_p - y_n)} \right] P_P = \frac{c_0}{(y_p - y_n)}$$

$$3. \frac{\alpha_{3n}}{(y_N - y_p)(y_p - y_n)} X_{1N} - \left[ \frac{\alpha_{3n}}{(y_N - y_p)(y_p - y_n)} + \frac{c_1}{(y_p - y_n)} \right] X_{1P}$$

$$+ \frac{\alpha_{3n}}{(y_N - y_p)(y_p - y_n)} X_{2N} - \left[ \frac{\alpha_{3n}}{(y_N - y_p)(y_p - y_n)} + \frac{c_2}{(y_p - y_n)} \right] X_{2P} + \frac{\beta_{3n}}{(y_N - y_p)(y_p - y_n)} P_N$$

$$+ \left[ \frac{\beta_{3n}}{(y_N - y_p)(y_p - y_n)} + \frac{c_3}{(y_p - y_n)} \right] P_P = \frac{c_0}{(y_p - y_n)}$$

For internal nodes present in Fig.5:

$$[N_x^e - N_x^w](y_s - y_n) + [N_y^n - N_y^s](x_w - x_e) = 0$$

$$\begin{aligned}
 1. \quad & \frac{\alpha_{1e}}{(x_E - x_p)(x_w - x_e)} X_{1E} + \frac{\alpha_{1w}}{(x_p - x_w)(x_w - x_e)} X_{1w} + \frac{\alpha_{1n}}{(y_N - y_p)(y_s - y_n)} X_{1N} + \\
 & \frac{\alpha_{1s}}{(y_p - y_s)(y_s - y_n)} X_{1s} - \left( \frac{\alpha_{1e}}{(x_E - x_p)(x_w - x_e)} + \frac{\alpha_{1w}}{(x_p - x_w)(x_w - x_e)} + \frac{\alpha_{1n}}{(y_N - y_p)(y_s - y_n)} \right. \\
 & \left. + \frac{\alpha_{1s}}{(y_p - y_s)(y_s - y_n)} \right) X_{1P} + \frac{\beta_{1e}}{(x_E - x_p)(x_w - x_e)} P_E + \frac{\beta_{1w}}{(x_p - x_w)(x_w - x_e)} P_w + \\
 & \frac{\beta_{1n}}{(y_N - y_p)(y_s - y_n)} P_N + \frac{\beta_{1s}}{(y_p - y_s)(y_s - y_n)} P_{1s} - \left( \frac{\beta_{1e}}{(x_E - x_p)(x_w - x_e)} + \right. \\
 & \left. \frac{\beta_{1w}}{(x_p - x_w)(x_w - x_e)} + \frac{\beta_{1n}}{(y_N - y_p)(y_s - y_n)} + \frac{\beta_{1s}}{(y_p - y_s)(y_s - y_n)} \right) P_P = 0
 \end{aligned}$$
  

$$\begin{aligned}
 2. \quad & \frac{\alpha_{2e}}{(x_E - x_p)(x_w - x_e)} X_{2E} + \frac{\alpha_{2w}}{(x_p - x_w)(x_w - x_e)} X_{2w} + \frac{\alpha_{2n}}{(y_N - y_p)(y_s - y_n)} X_{2N} + \\
 & \frac{\alpha_{2s}}{(y_p - y_s)(y_s - y_n)} X_{2s} - \left( \frac{\alpha_{2e}}{(x_E - x_p)(x_w - x_e)} + \frac{\alpha_{2w}}{(x_p - x_w)(x_w - x_e)} + \frac{\alpha_{2n}}{(y_N - y_p)(y_s - y_n)} \right. \\
 & \left. + \frac{\alpha_{2s}}{(y_p - y_s)(y_s - y_n)} \right) X_{2P} + \frac{\beta_{2e}}{(x_E - x_p)(x_w - x_e)} P_E + \frac{\beta_{2w}}{(x_p - x_w)(x_w - x_e)} P_w + \\
 & \frac{\beta_{2n}}{(y_N - y_p)(y_s - y_n)} P_N + \frac{\beta_{2s}}{(y_p - y_s)(y_s - y_n)} P_{2s} - \left( \frac{\beta_{2e}}{(x_E - x_p)(x_w - x_e)} + \right. \\
 & \left. \frac{\beta_{2w}}{(x_p - x_w)(x_w - x_e)} + \frac{\beta_{2n}}{(y_N - y_p)(y_s - y_n)} + \frac{\beta_{2s}}{(y_p - y_s)(y_s - y_n)} \right) P_P = 0
 \end{aligned}$$

$$\begin{aligned}
3. \quad & \frac{\alpha_{3e}}{(x_E - x_p)(x_w - x_e)} X_{1E} + \frac{\alpha_{3w}}{(x_p - x_w)(x_w - x_e)} X_{1w} + \frac{\alpha_{3n}}{(y_N - y_p)(y_s - y_n)} X_{1N} + \\
& \frac{\alpha_{3s}}{(y_p - y_s)(y_s - y_n)} X_{1s} - \left( \frac{\alpha_{3e}}{(x_E - x_p)(x_w - x_e)} + \frac{\alpha_{3w}}{(x_p - x_w)(x_w - x_e)} + \frac{\alpha_{3n}}{(y_N - y_p)(y_s - y_n)} \right. \\
& \left. + \frac{\alpha_{3s}}{(y_p - y_s)(y_s - y_n)} \right) X_{1P} + \frac{\alpha_{3e}}{(x_E - x_p)(x_w - x_e)} X_{2E} + \frac{\alpha_{3w}}{(x_p - x_w)(x_w - x_e)} X_{2w} + \\
& \frac{\alpha_{3n}}{(y_N - y_p)(y_s - y_n)} X_{2N} + \frac{\alpha_{3s}}{(y_p - y_s)(y_s - y_n)} X_{2s} - \left( \frac{\alpha_{3e}}{(x_E - x_p)(x_w - x_e)} + \right. \\
& \left. \frac{\alpha_{3w}}{(x_p - x_w)(x_w - x_e)} + \frac{\alpha_{3n}}{(y_N - y_p)(y_s - y_n)} + \frac{\alpha_{3s}}{(y_p - y_s)(y_s - y_n)} \right) X_{2P} + \\
& \frac{\beta_{3e}}{(x_E - x_p)(x_w - x_e)} P_E + \frac{\beta_{3w}}{(x_p - x_w)(x_w - x_e)} P_w + \frac{\beta_{3n}}{(y_N - y_p)(y_s - y_n)} P_N + \\
& \frac{\beta_{3s}}{(y_p - y_s)(y_s - y_n)} P_{1s} - \left( \frac{\beta_{3e}}{(x_E - x_p)(x_w - x_e)} + \frac{\beta_{3w}}{(x_p - x_w)(x_w - x_e)} + \frac{\beta_{3n}}{(y_N - y_p)(y_s - y_n)} + \right. \\
& \left. + \frac{\beta_{3s}}{(y_p - y_s)(y_s - y_n)} \right) P_P = 0
\end{aligned}$$

For the nodes present on right boundary of Fig.5:

$$[N_x^e - N_x^w](y_s - y_n) + [N_y^n - N_y^s](x_w - x_e) = 0$$

Applying image point technique,  $N_x^e = -N_x^w$

$$\begin{aligned}
 1. \quad & \frac{2\alpha_{1w}}{(x_p - x_w)(x_w - x_e)} X_{1w} + \frac{\alpha_{1n}}{(y_N - y_p)(y_s - y_n)} X_{1n} + \frac{\alpha_{1s}}{(y_p - y_s)(y_s - y_n)} X_{1s} - \\
 & \left( \frac{2\alpha_{1w}}{(x_p - x_w)(x_w - x_e)} + \frac{\alpha_{1n}}{(y_N - y_p)(y_s - y_n)} + \frac{\alpha_{1s}}{(y_p - y_s)(y_s - y_n)} \right) X_{1p} + \\
 & \frac{\beta_{1e}}{(x_E - x_p)(x_w - x_e)} P_E + \frac{2\beta_{1w}}{(x_p - x_w)(x_w - x_e)} P_w + \frac{\beta_{1n}}{(y_N - y_p)(y_s - y_n)} P_n + \\
 & \frac{\beta_{1s}}{(y_p - y_s)(y_s - y_n)} P_{1s} - \left( \frac{\beta_{1e}}{(x_E - x_p)(x_w - x_e)} + \frac{2\beta_{1w}}{(x_p - x_w)(x_w - x_e)} + \frac{\beta_{1n}}{(y_N - y_p)(y_s - y_n)} \right. \\
 & \left. + \frac{\beta_{1s}}{(y_p - y_s)(y_s - y_n)} \right) P_p = 0
 \end{aligned}$$

$$\begin{aligned}
 2. \quad & \frac{2\alpha_{2w}}{(x_p - x_w)(x_w - x_e)} X_{2w} + \frac{\alpha_{2n}}{(y_N - y_p)(y_s - y_n)} X_{2n} + \frac{\alpha_{2s}}{(y_p - y_s)(y_s - y_n)} X_{2s} - \\
 & \left( \frac{2\alpha_{2w}}{(x_p - x_w)(x_w - x_e)} + \frac{\alpha_{2n}}{(y_N - y_p)(y_s - y_n)} + \frac{\alpha_{2s}}{(y_p - y_s)(y_s - y_n)} \right) X_{2p} + \\
 & \frac{2\beta_{2w}}{(x_p - x_w)(x_w - x_e)} P_w + \frac{\beta_{2n}}{(y_N - y_p)(y_s - y_n)} P_n + \frac{\beta_{2s}}{(y_p - y_s)(y_s - y_n)} P_{2s} - \\
 & \left( \frac{2\beta_{2w}}{(x_p - x_w)(x_w - x_e)} + \frac{\beta_{2n}}{(y_N - y_p)(y_s - y_n)} + \frac{\beta_{2s}}{(y_p - y_s)(y_s - y_n)} \right) P_p = 0
 \end{aligned}$$

$$\begin{aligned}
3. \quad & \frac{2\alpha_{3w}}{(x_p - x_w)(x_w - x_e)} X_{1w} + \frac{\alpha_{3n}}{(y_N - y_p)(y_s - y_n)} X_{1n} + \frac{\alpha_{3s}}{(y_p - y_s)(y_s - y_n)} X_{1s} \\
& \left( \frac{2\alpha_{3w}}{(x_p - x_w)(x_w - x_e)} + \frac{\alpha_{3n}}{(y_N - y_p)(y_s - y_n)} + \frac{\alpha_{3s}}{(y_p - y_s)(y_s - y_n)} \right) X_{1p} + \\
& \frac{2\alpha_{3w}}{(x_p - x_w)(x_w - x_e)} X_{2w} + \frac{\alpha_{3n}}{(y_N - y_p)(y_s - y_n)} X_{2n} + \frac{\alpha_{3s}}{(y_p - y_s)(y_s - y_n)} X_{2s} \\
& \left( \frac{2\alpha_{3w}}{(x_p - x_w)(x_w - x_e)} + \frac{\alpha_{3n}}{(y_N - y_p)(y_s - y_n)} + \frac{\alpha_{3s}}{(y_p - y_s)(y_s - y_n)} \right) X_{2p} + \\
& \frac{2\beta_{3w}}{(x_p - x_w)(x_w - x_e)} P_w + \frac{\beta_{3n}}{(y_N - y_p)(y_s - y_n)} P_n + \frac{\beta_{3s}}{(y_p - y_s)(y_s - y_n)} P_{is} \\
& \left( \frac{2\beta_{3w}}{(x_p - x_w)(x_w - x_e)} + \frac{\beta_{3n}}{(y_N - y_p)(y_s - y_n)} + \frac{\beta_{3s}}{(y_p - y_s)(y_s - y_n)} \right) P_p = 0
\end{aligned}$$

## CHAPTER 3

### RESULTS AND DISCUSSION

The computed growth profiles for blanket tungsten CVD are discussed in this chapter. The values of parameters used in calculating the growth profile of W deposition process is given in Table 1. While  $L_0$  is always  $2\mu\text{m}$ , we change the aspect ratio, which is the depth divided by the half-width of the trench, by varying  $W_0$  between  $0.2\mu\text{m}$  and  $0.5\mu\text{m}$ .

**Table 1: Values of parameters used in computing results**

Density of tungsten, $\rho_W$ , gm/cc	19.22
Molecular weight of tungsten, $M_W$ , g/mole	183.85
Constant used in rate expression for tungsten deposition, $k_f$ , (dynes/cm <sup>2</sup> ) <sup>-1</sup>	0.75006
Mole fraction of $\text{H}_2$ , $X_1^0$	0.9615
Mole fraction of $\text{WF}_6$ , $X_2^0$	0.0384
Mole fraction of $\text{HF}$ , $X_3^0$	0.0
Total pressure, $P^0$ , dynes/cm <sup>2</sup>	1333.2
Depth of the trench, $L_0$ , $\mu\text{m}$	2.0

For calculating binary diffusion coefficient and viscosity (as given in Appendix I), we need Lennard-Jones parameters and values of collision integrals,  $\Omega^{11}$  and  $\Omega^{22}$ . The lennard-Jones parameters are provided in Table 2[11], whereas the values of  $\Omega^{11}$  and  $\Omega^{22}$

are interpolated at the corresponding  $T^*$  ( $=k_B T/\epsilon$ ) by using standard table[30] for collision integral.

**Table 2: Lennard-Jones parameters**

$\sigma, H_2, \text{ \AA}^0$	2.827
$\epsilon/k_B, H_2, \text{ K}$	59.7
$\sigma, WF_6, \text{ \AA}^0$	5.21
$\epsilon/k_B, WF_6, \text{ K}$	338
$\sigma, HF, \text{ \AA}^0$	3.15
$\epsilon/k_B, HF, \text{ K}$	330

First sets of results are on comparison of mesh. For this we have taken a trench of width  $W_0=0.35\mu\text{m}$  at 773 K. the computational domain is divided into 100 interval both in X and Y direction. The progression of deposition of time is depicted in Fig.1. In plotting this and subsequent similar figures, we have shifted the origin to center of the trench base (see Fig.2).

Also, the various deposition profiles are for increasing time,  $\tau$ , expressed as actual time divided by total processing time; the process is deemed over when  $W/W_0$  is zero at  $L/L_0=1$ . The plotted profiles are for  $\tau$  ranging from 0 to 1, in intervals of 0.1.

The results in Fig.1 demonstrate that in the initial deposition period, the trench fills uniformly. However, as the trench width becomes small, process becomes mass transport limited, and a concentration gradient sets in. Hence the trench entrance fills faster, eventually leading to a void.

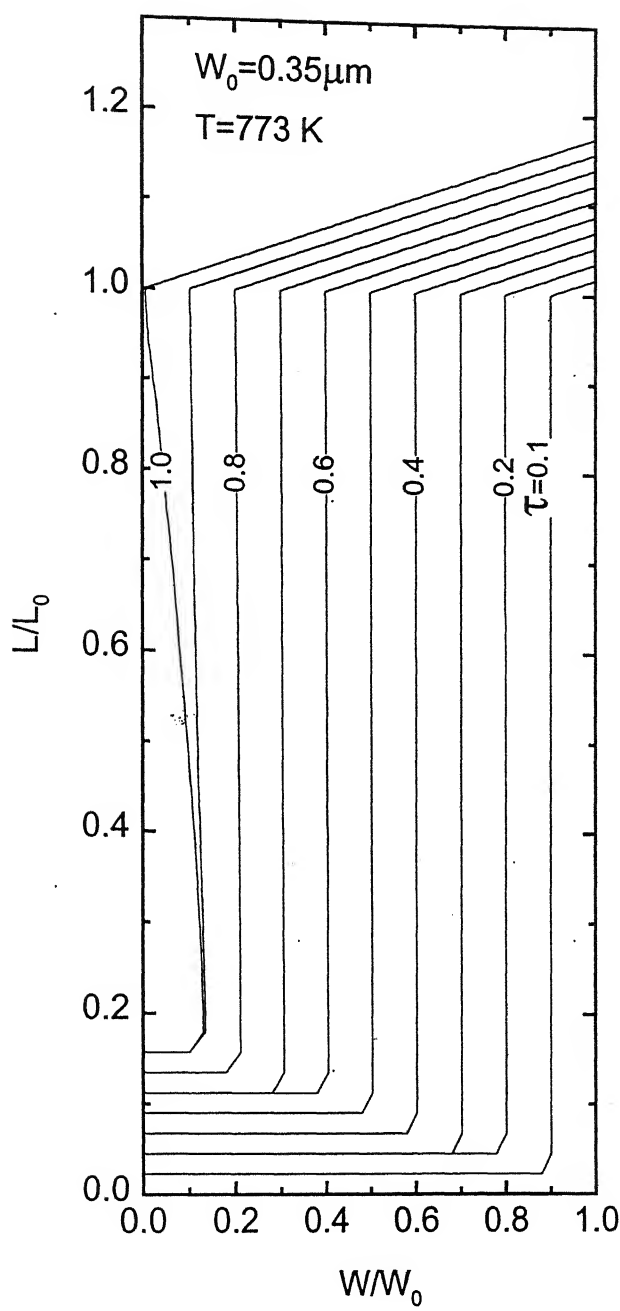


Fig.1: Isothermal deposition profile at 773 K for  $W_0 = 0.35\mu\text{m}$  and mesh size 101x101; total processing time is 40 seconds

The formation of a void is consistent with both experimental observation[17] and modeling of it[9,23]. In order to determine the mesh sensitivity in our calculations, we next divided the domain in 50 intervals, instead of 100, in both X and Y directions.

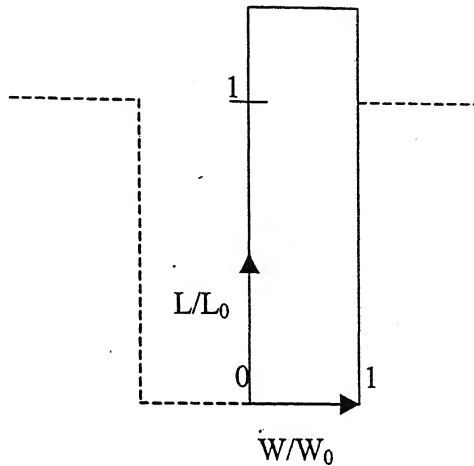


Fig.2: Schematic of a trench corresponding to Fig.1.

The formation of a void is consistent with both experimental observation[17] and modeling of it[9,23]. In order to determine the mesh sensitivity in our calculations, we next divided the domain in 50 intervals, instead of 100, in both X and Y directions. The result for this case, in Fig.3, is compared with that in Fig.1. We find no significant difference between the two; the normalized void volume, defined as volume of the void divided by initial trench volume, is 7.0% and 6.7% for cases in Fig.1 and Fig.3, respectively. Since this difference is not significant, and that it took 4 hrs and 30 minutes of real time on a pentium II machine with 50x50 mesh, while 3 days and 18 hrs in the case of 100x100 mesh, in all subsequent calculations, the mesh used is the same as in Fig.3.

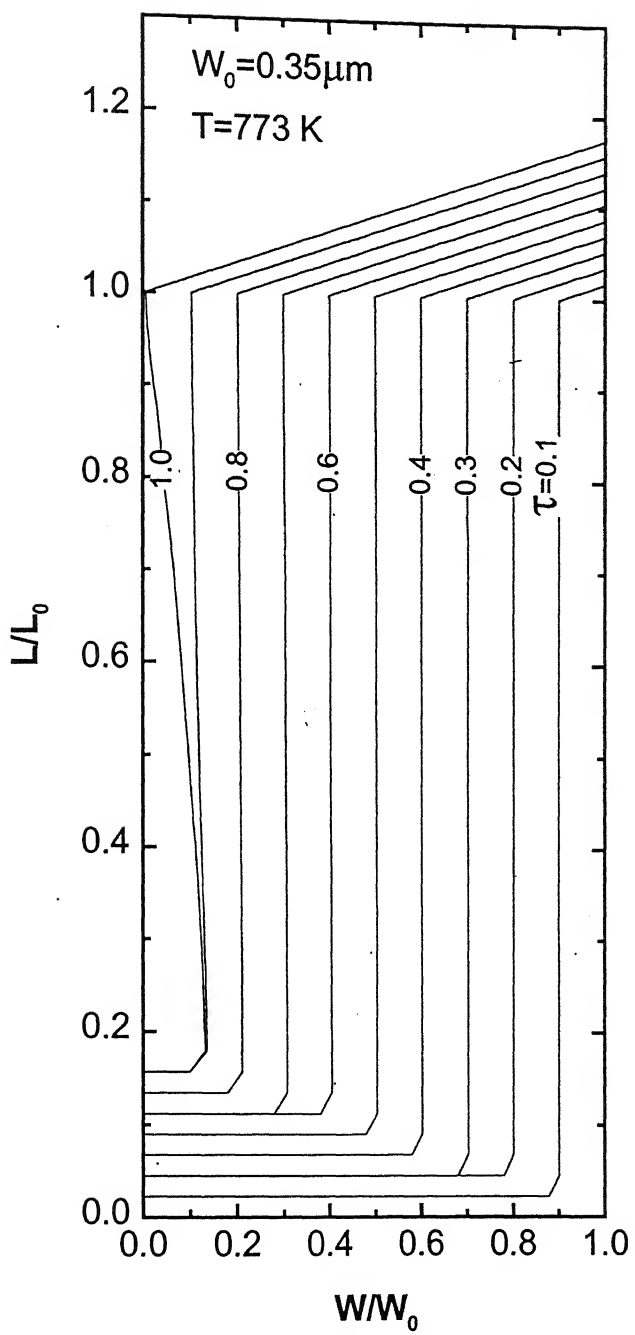


Fig.3: Isothermal deposition profile at 773 K for  $W_0 = 0.35\mu\text{m}$   
and for a mesh 51x51; total processing time is 40 seconds

### 3.1 DEPOSITION AT 773 K

The first few computations are for W deposition under isothermal conditions. In addition to results presented in Fig.3, at a deposition temperature of 773 K, which is regarded as an upper limit of deposition temperature, the simulation is performed for three additional trench widths  $0.2\mu\text{m}$ ,  $0.25\mu\text{m}$  and  $0.5\mu\text{m}$ .

Fig.4 depicts the growth profile for a trench  $0.5\mu\text{m}$  wide, where a void is found to be formed having a normalized void volume 3.4%. Thus the normalized void volume increases from 3.4 to 6.7 as trench width decreases from  $0.5\mu\text{m}$  to  $0.35\mu\text{m}$  (see Fig.3). A further increase in the void formation is noticed when  $W_0$  decreases to  $0.25\mu\text{m}$  and  $0.2\mu\text{m}$ . Fig.5 and 6 show the simulated growth profiles for trench width  $0.25\mu\text{m}$  and  $0.2\mu\text{m}$ . The corresponding normalized void volumes are 12.2% and 17.3%, respectively.

Thus, at a deposition temperature 773 K, a significant void forms in all the cases. This is due to the concentration gradient that develops along the vertical direction of the trench. Since, the reaction rate is dependent on concentration of reacting species, the mouth of the trench fills faster. Thus, once the trench entrance is closed, a void forms.

Also, the normalized void volume increases, as the aspect ratio of the trench increases. Clearly, as the trench width decreases, more resistance is offered to the diffusion of reacting species, which, in turn, shifts the deposition process to mass transfer control. As a result, stiffer concentration gradient is set in vertical direction. This leads to a more rapid mouth closure in high aspect ratio trenches.

In prelude to this work, we have suggested that imposing a temperature gradient may alleviate the problem of void formation. If due to concentration gradient, the reaction rate is faster at the trench entrance than at the bottom of the trench, we impose a

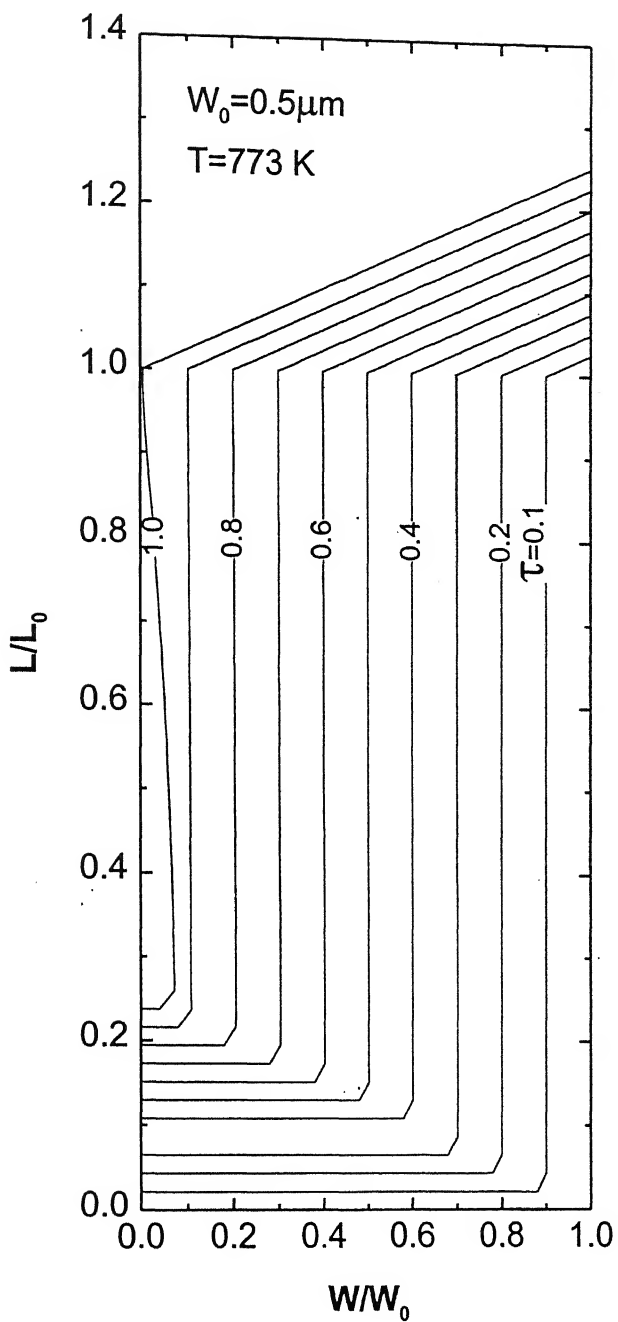


Fig.4: Isothermal deposition profile at 773 K for  $W_0 = 0.5 \mu\text{m}$ ;  
total processing time is 57 seconds

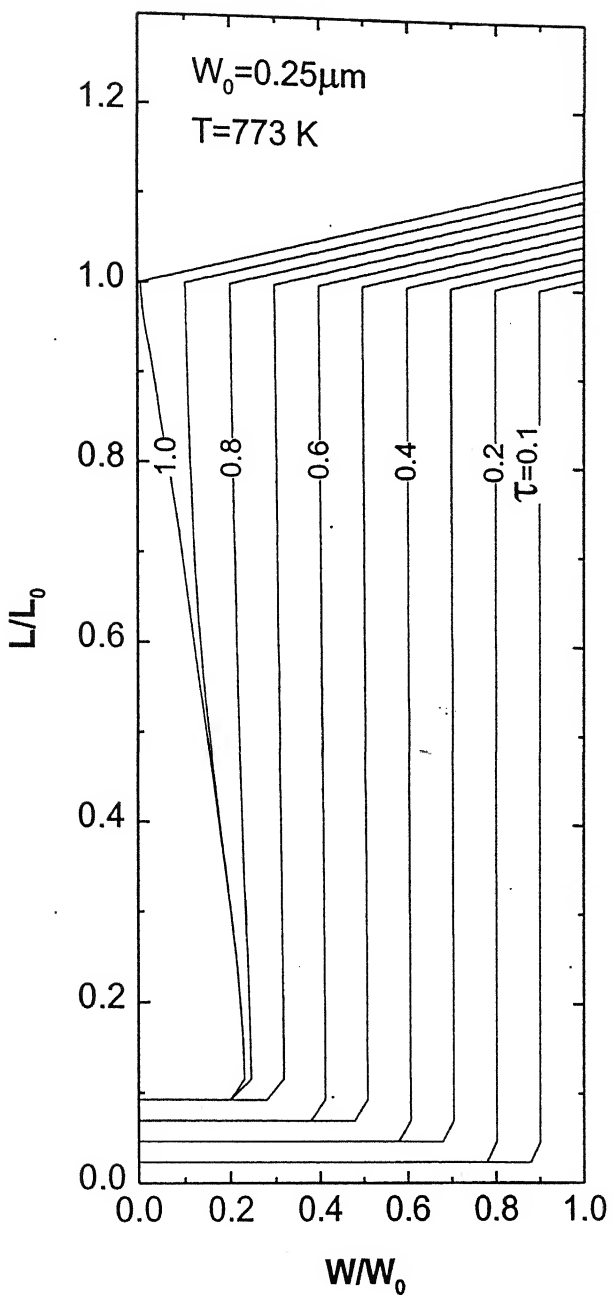


Fig.5: Isothermal deposition profile at 773 K for  $W_0 = 0.25\mu\text{m}$ ;  
total processing time is 28 seconds

temperature gradient along the depth of the trench with higher temperature at the bottom than at the entrance. This would compensate for lower deposition rate at the bottom of the trench. Here, in all four cases, we kept the entrance of the trench at 773 K, but linearly increase the temperature to the bottom by 3 K; no temperature gradient is imposed in X direction. After every successive growth step, the depth of the trench increases and again the mouth temperature is fixed at 773 K. The simulated profiles are shown in Fig.7 through 10. These figures depict that, in no case, by imposing a temperature gradient avoids void formation. However, we are able to decrease the normalized trench volume in all the cases. The normalized trench volumes are decreased from 3.5, 6.7, 12.2 and 17.3% to corresponding values 2.1, 5.3, 10.7 and 16.1% for trench  $0.5\mu\text{m}$ ,  $0.35\mu\text{m}$ ,  $0.25\mu\text{m}$  and  $0.2\mu\text{m}$  wide, respectively. Thus from the discussions so far, it is obvious that 773 K is not an ideal deposition temperature for W CVD. It would be possible to impose a steeper temperature gradient in order to completely fill the void. But such gradients may be difficult to obtain. Thus we fix the maximum difference of temperature ( $\Delta T$ ) between entrance and bottom of trench to 3 K, and examine void formation at a lower temperature.

### 3.2 DEPOSITION AT 673 K

Few simulations are performed at a deposition temperature 673 K. In Fig.11 we represent the isothermal profile for a trench of width  $0.5\mu\text{m}$ . Now the normalized void volume is 0.5%, much lower than 3.4% at 773 K. Similarly, in Fig.12-14, we show the growth profile at 673 K for trench widths  $0.35\mu\text{m}$ ,  $0.25\mu\text{m}$  and  $0.2\mu\text{m}$ , respectively. The

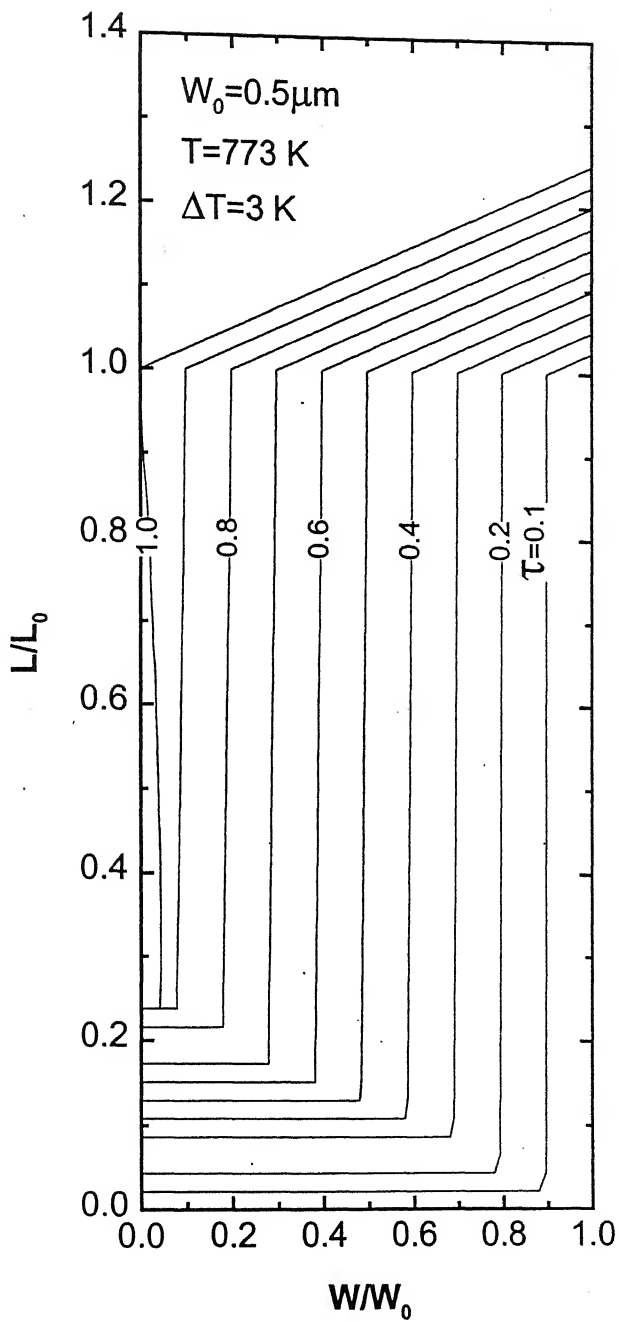


Fig.7: Modified deposition profile of Fig.4 under non-isothermal condition; total processing time is 57 seconds

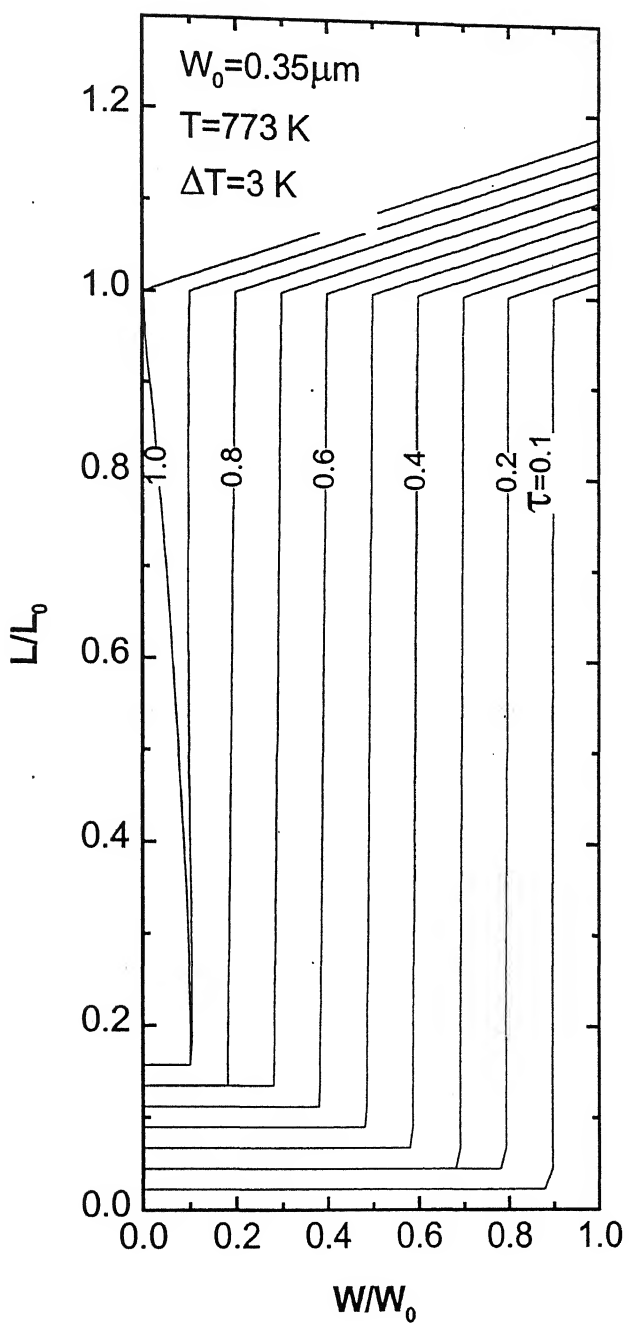


Fig.8: Modified deposition profile of Fig.3 under non-isothermal condition; total processing time is 40 seconds

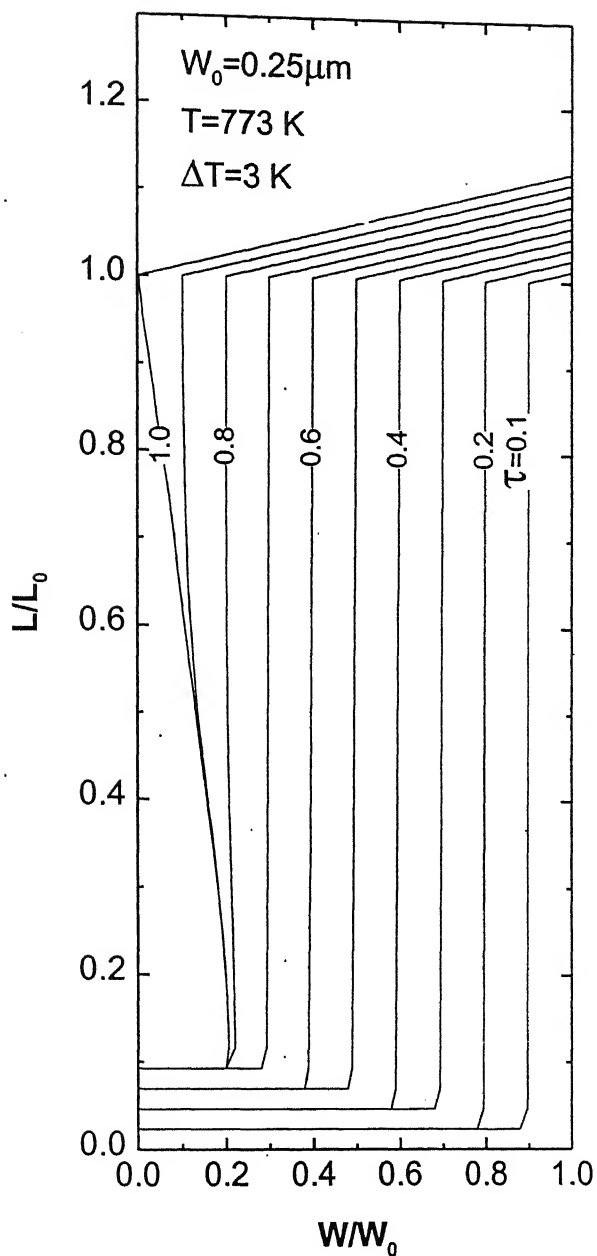


Fig.9: Modified deposition profile of Fig.5 under non-isothermal condition; total processing time is 28 seconds

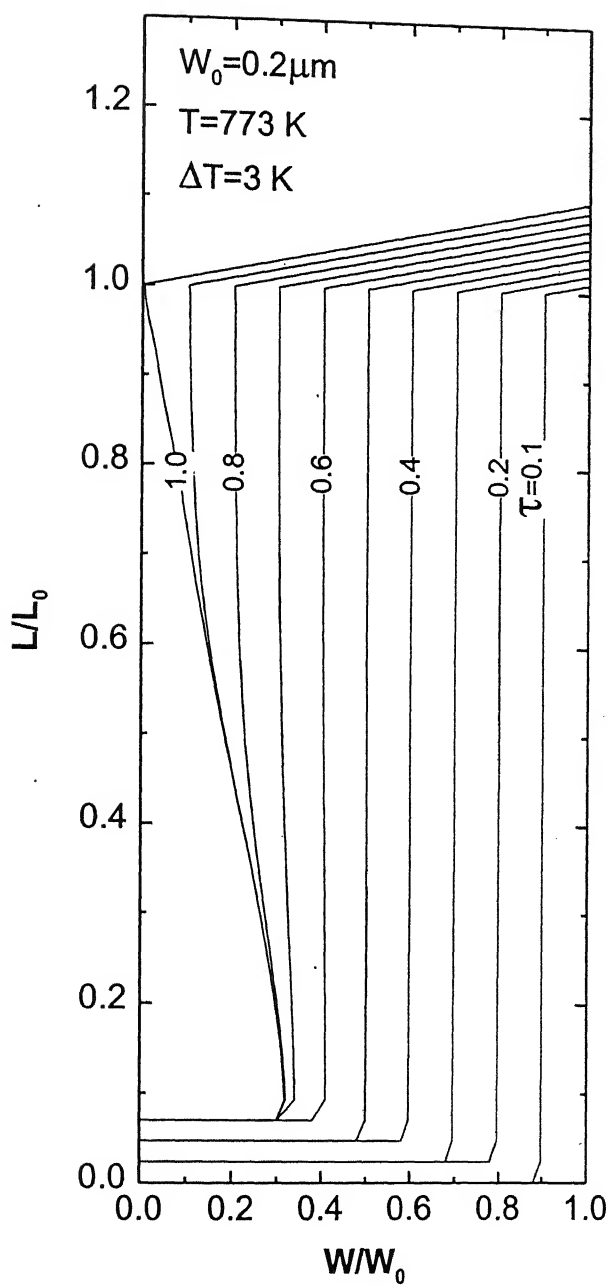


Fig.10: Modified deposition profile of Fig.6 under non-isothermal condition; total processing time is 23 seconds

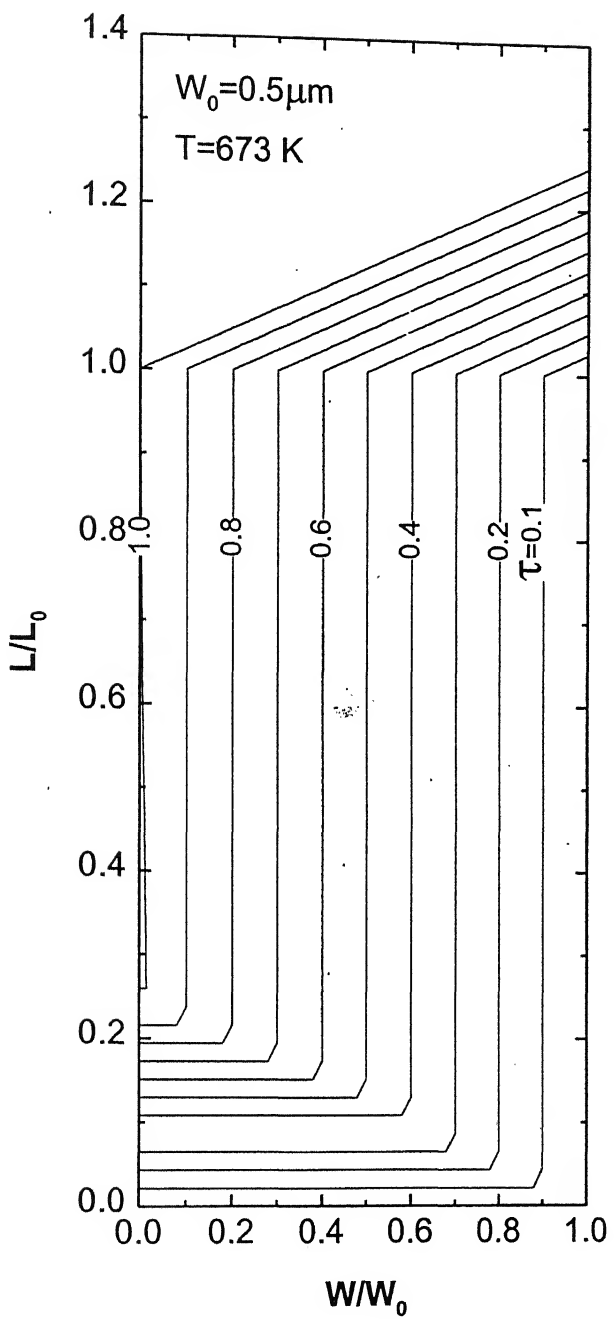


Fig.11: Isothermal deposition profile at 673 K for W<sub>0</sub>=0.5μm;  
total deposition time is 308 seconds

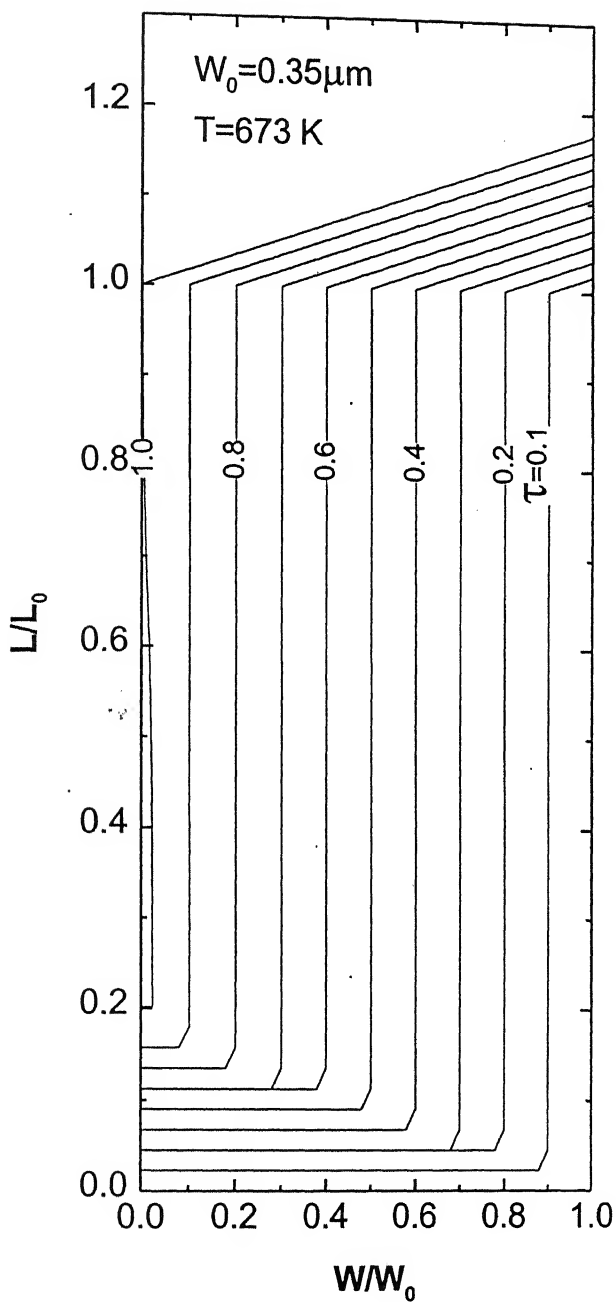


Fig.12: Isothermal deposition profile at 673 K for  $W_0 = 0.35\mu\text{m}$ ;  
total deposition time is 215 seconds

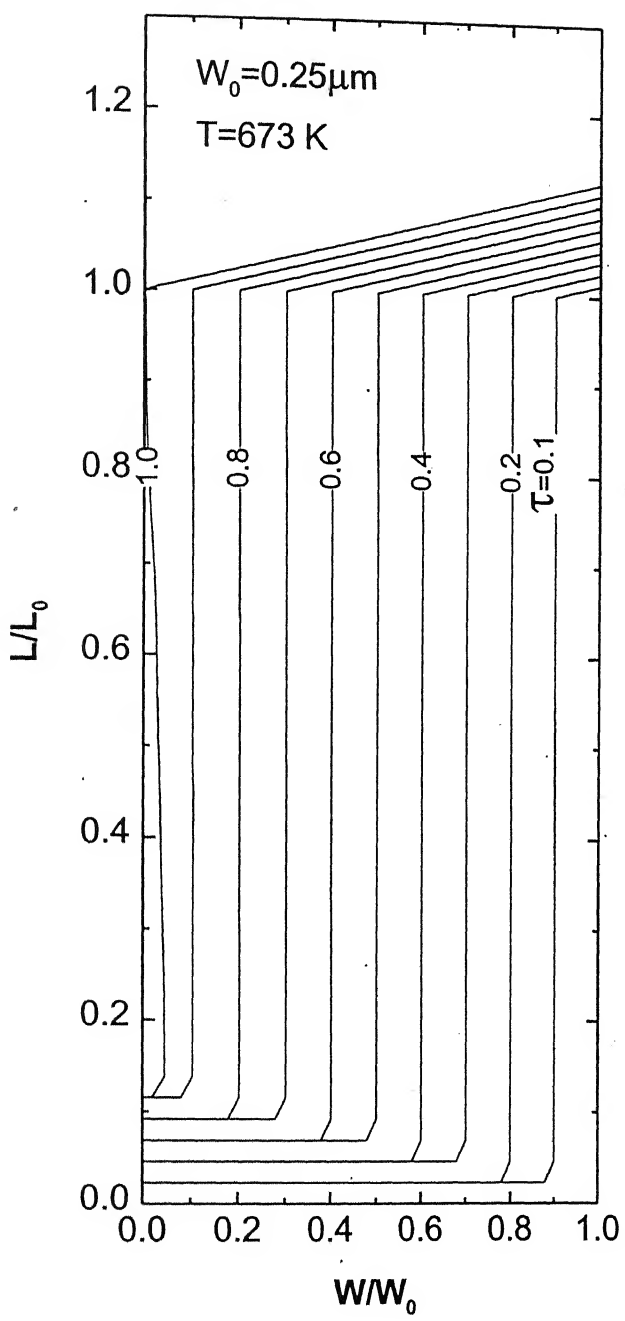


Fig.13: Isothermal deposition profile at 673 K for  $W_0 = 0.25\mu\text{m}$ ;  
 total deposition time is 154 seconds

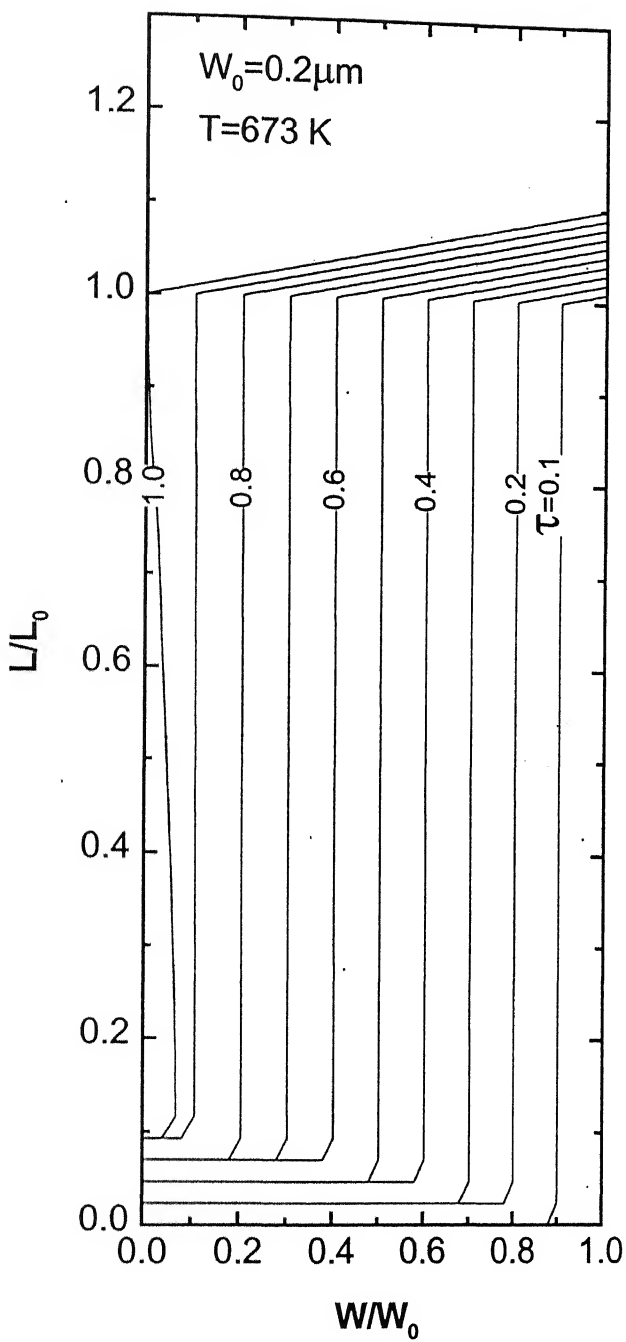


Fig.14: Isothermal deposition profile at 673 K for  $W_0 = 0.2\mu\text{m}$ ;  
total deposition time is 123 seconds

corresponding normalized void volumes are 1.2%, 2.4% and 3.5%. These values are also much lower than the void volume at 773 K.

However, also at 673 K, a void forms in all cases discussed here. However, the normalized void volume is comparatively lesser, when compared to the corresponding cases at 773 K. That means, for a particular aspect ratio, the normalized trench volume increases with an increase in temperature. Clearly, with increase in deposition temperature, the reaction rate increases exponentially while the diffusion constants increase by a smaller power of temperature. Thus the reaction kinetics becomes faster allowing the deposition process to shift further to mass transport controlled regime; as a result, keyholes are formed which are larger in volume than those formed at lower deposition temperatures.

Here at 673 K also, a controlled thermal gradient is applied in the vertical direction of the trench (as in the cases for 773 K). As depicted in Fig.15, for a trench width of  $0.5\mu\text{m}$ , only 1 K temperature difference between entrance and the bottom of the trench is sufficient to ensure complete filling of the trench. But, for the trench width  $0.35\mu\text{m}$  (see Fig.16), 2 K temperature difference is needed for void-free deposition. However, for trench widths  $0.25\mu\text{m}$  and  $0.2\mu\text{m}$ , as shown in Fig.17 and Fig.18, respectively, we need a temperature difference of 3 K for complete filling.

The results clearly demonstrate that the imposition of controlled thermal gradient can be employed to completely fill the trenches.

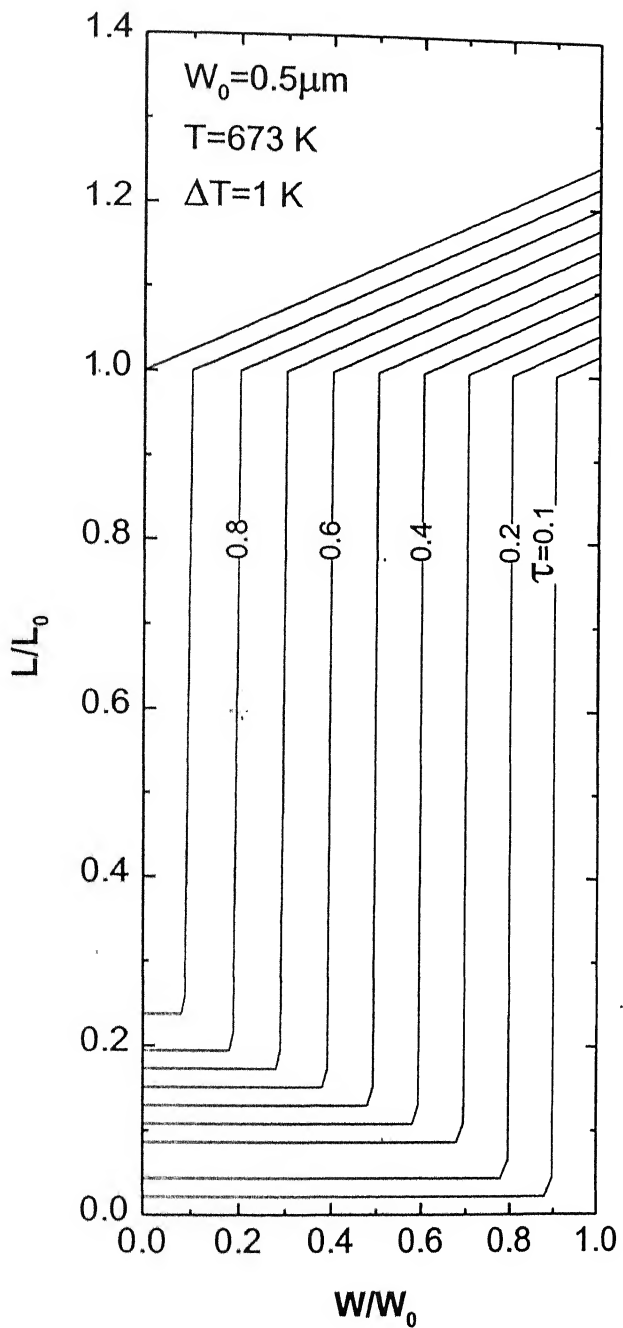


Fig.15: Modified deposition profile of Fig.11 after application of  $\Delta T=1$  K;  
total processing time is 307 seconds

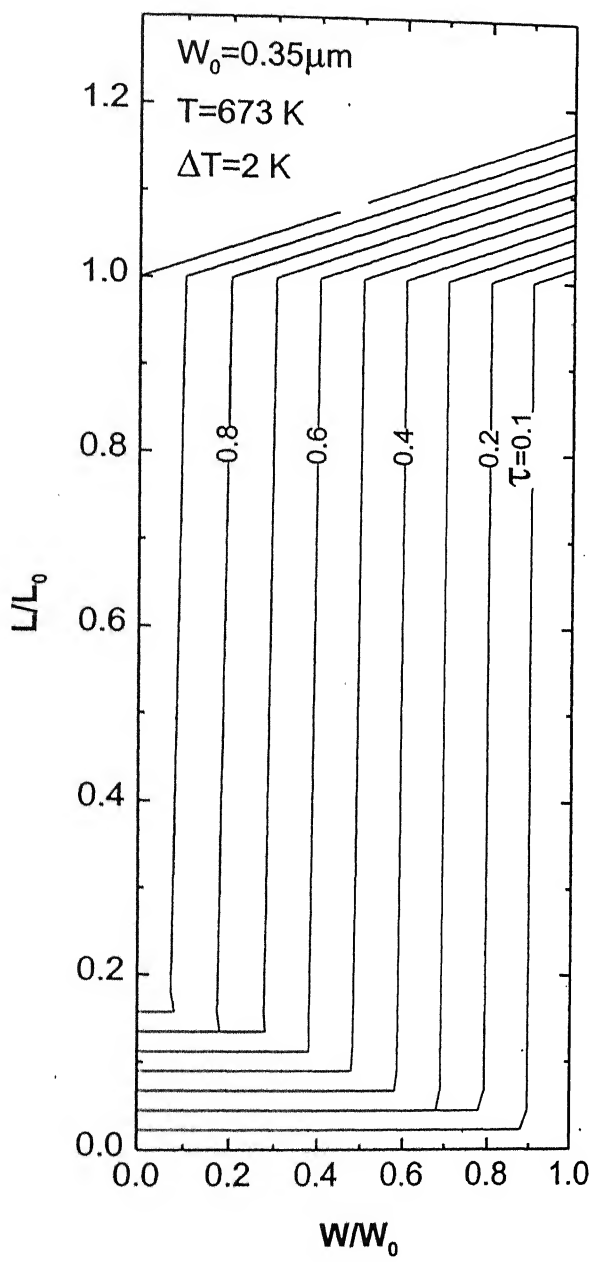


Fig. 16: Modified deposition profile of Fig. 12 after application of  $\Delta T = 2\text{ K}$ ;  
total processing time is 215 seconds

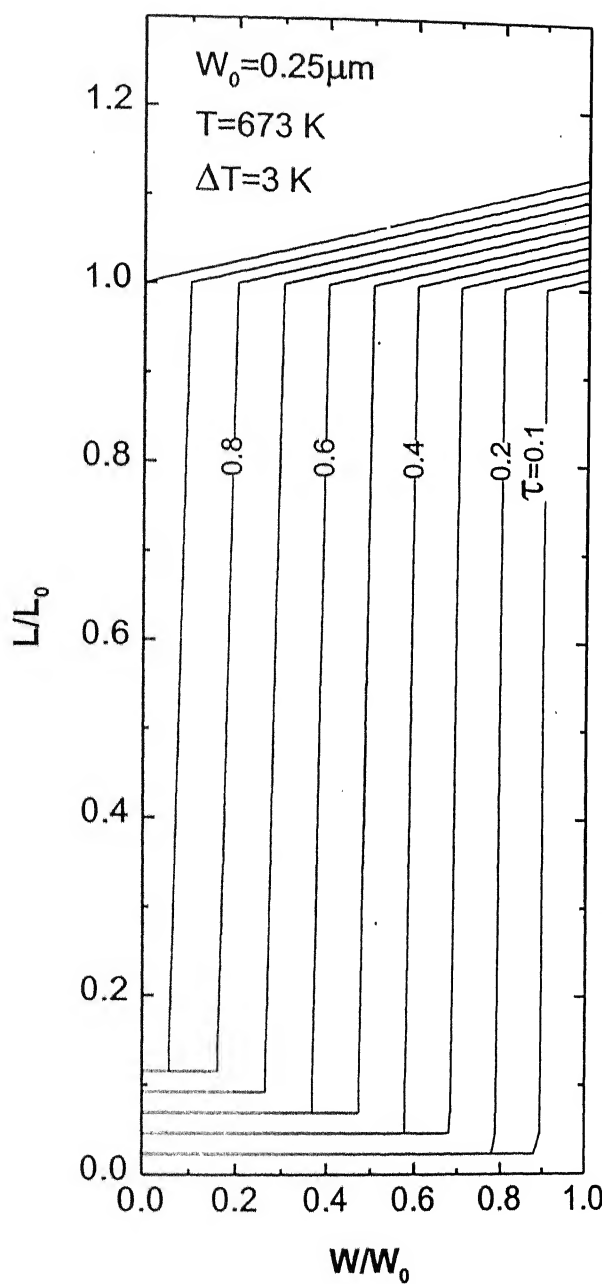


Fig.17: Modified deposition profile of Fig.13 after application of  $\Delta T = 3\text{ K}$ ;  
 total processing time is 154 seconds

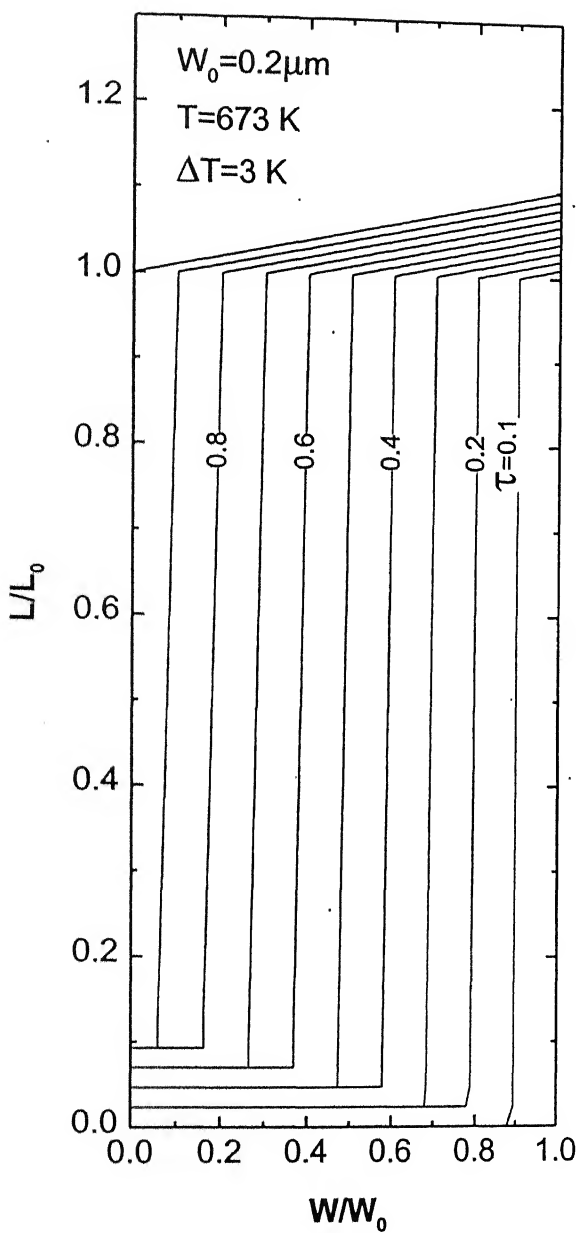


Fig.18: Modified deposition profile of Fig.14 after application of  $\Delta T = 3\text{ K}$ ;  
total processing time is 123 seconds

### 3.3 DEPOSITION AT 573 K

Indeed, just as going from 773 K to 673 K lead to reduction in normalized void volume, a further reduction in temperature for isothermal CVD could also ensure complete filling of the trench. This is demonstrated by reducing the deposition temperature to 573 K.

In all four cases corresponding to  $W_0=0.5, 0.35, 0.25$  and  $0.2\mu\text{m}$ , a completely filled trench is achieved without any application of thermal gradient (see Fig.19-22). Thus it has been necessary to conduct CVD at a lower temperature to bring deposition under kinetic control and hence uniform deposition. However, this requires longer processing time, and hence longer through put.

Thus we have shown for the first time that by application of temperature gradient, it will be possible to fill a trench at a higher temperature. This would result in an increased through put.

### 3.3 THE THERMAL GRADIENT

In this work so far, we have proposed a maximum gradient of  $1.5\text{K}/\mu\text{m}$ . We now discuss the feasibility of supporting such a temperature gradient.

First we assume that the gases in the trench are in thermal equilibrium with the neighboring dielectric. If the wafer loses heat by convection from the top surface, then the heat transfer at  $t=0$  is defined according to,

$$K_{\text{diel}} \frac{\Delta T}{L_0} = h(T_s - 298),$$

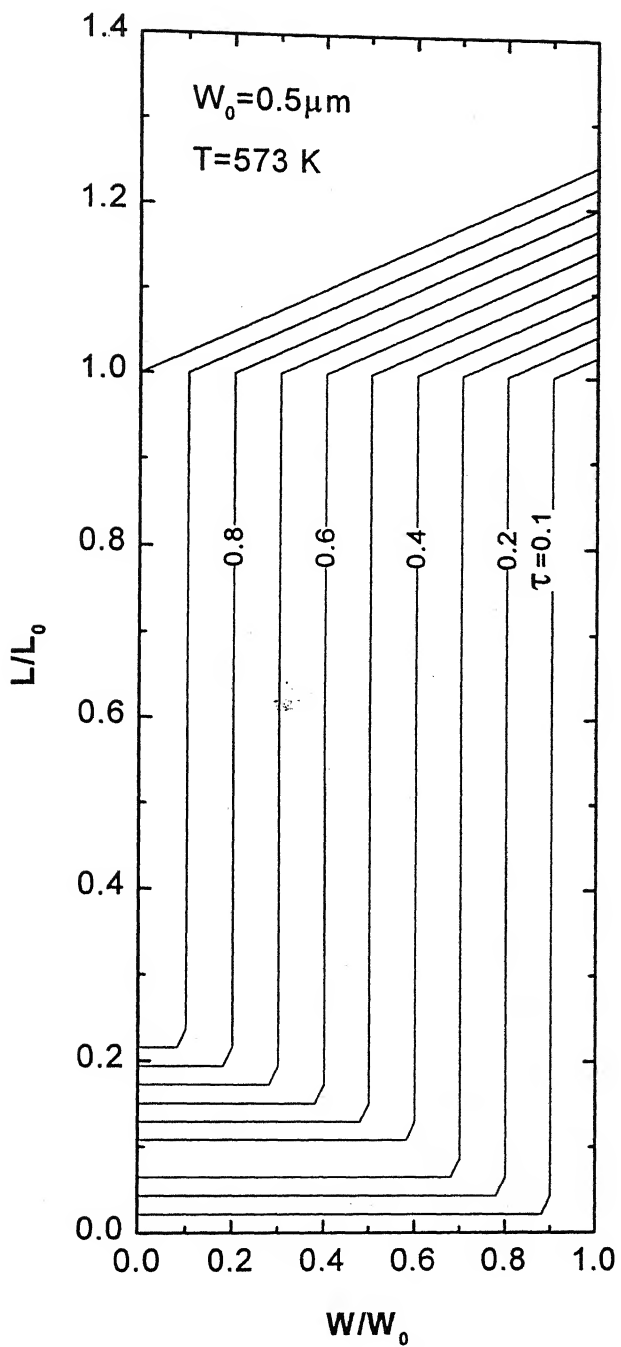


Fig.19: Isothermal deposition profile at 573 K for W<sub>0</sub>=0.5 μm;  
total deposition time is 3004 seconds

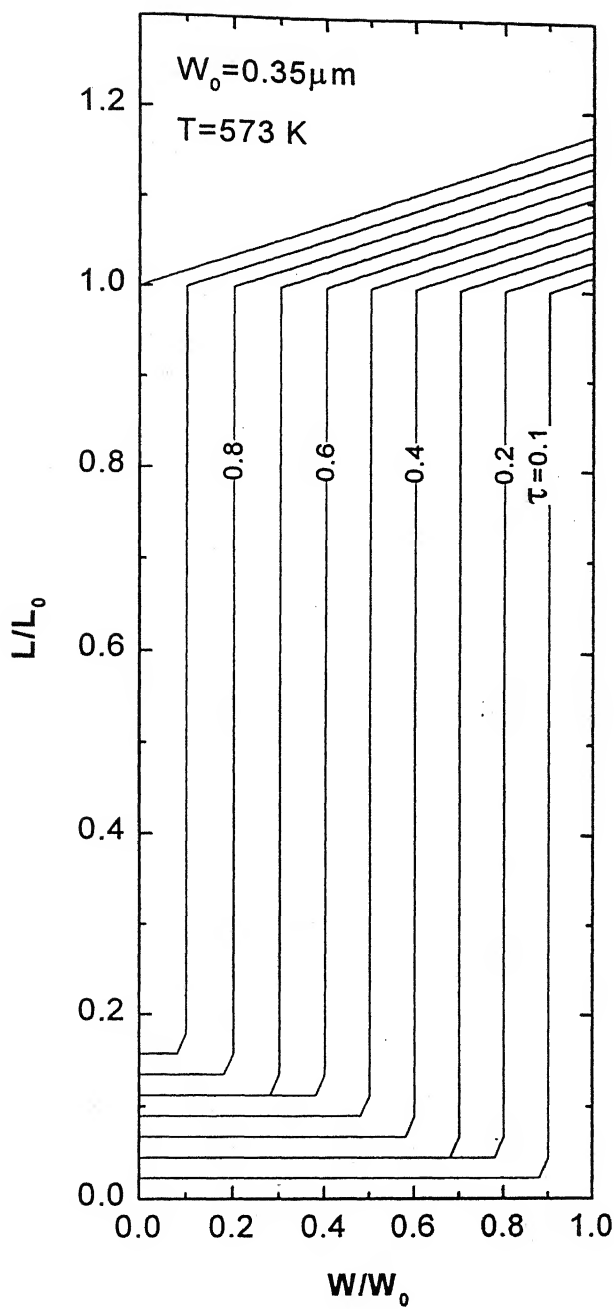


Fig.20: Isothermal deposition profile at 573 K for  $W_0 = 0.35\mu\text{m}$ ;  
total deposition time is 2103 seconds

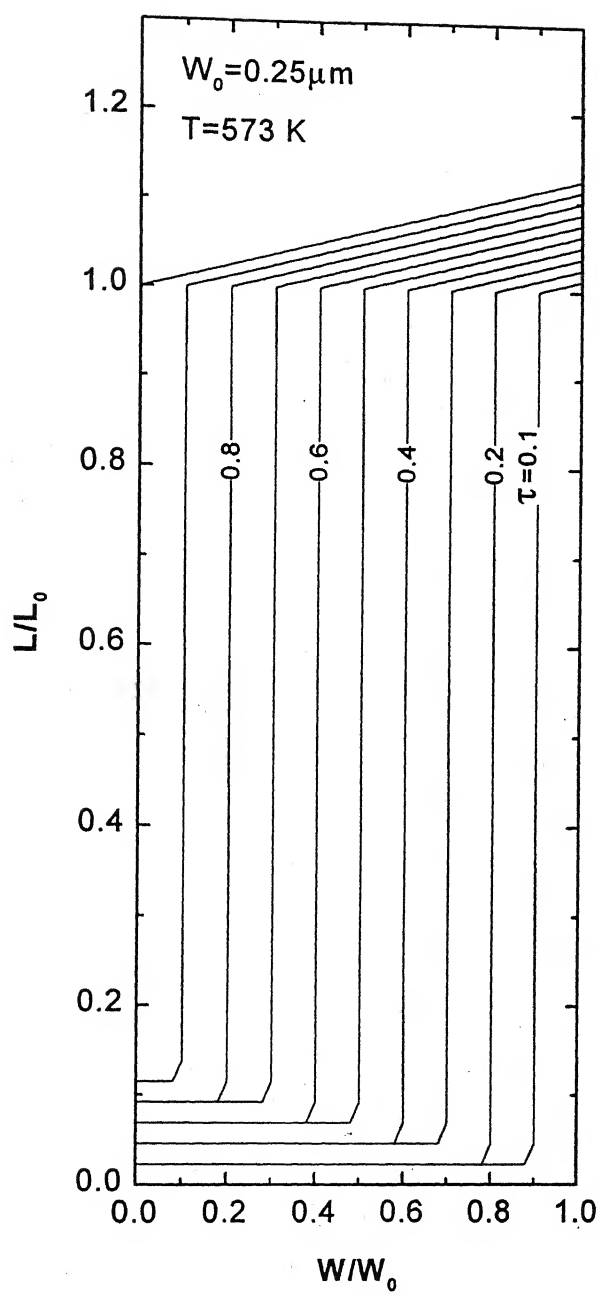


Fig.21: Isothermal deposition profile at 573 K for  $W_0 = 0.25 \mu\text{m}$ ;  
total deposition time is 1507 seconds

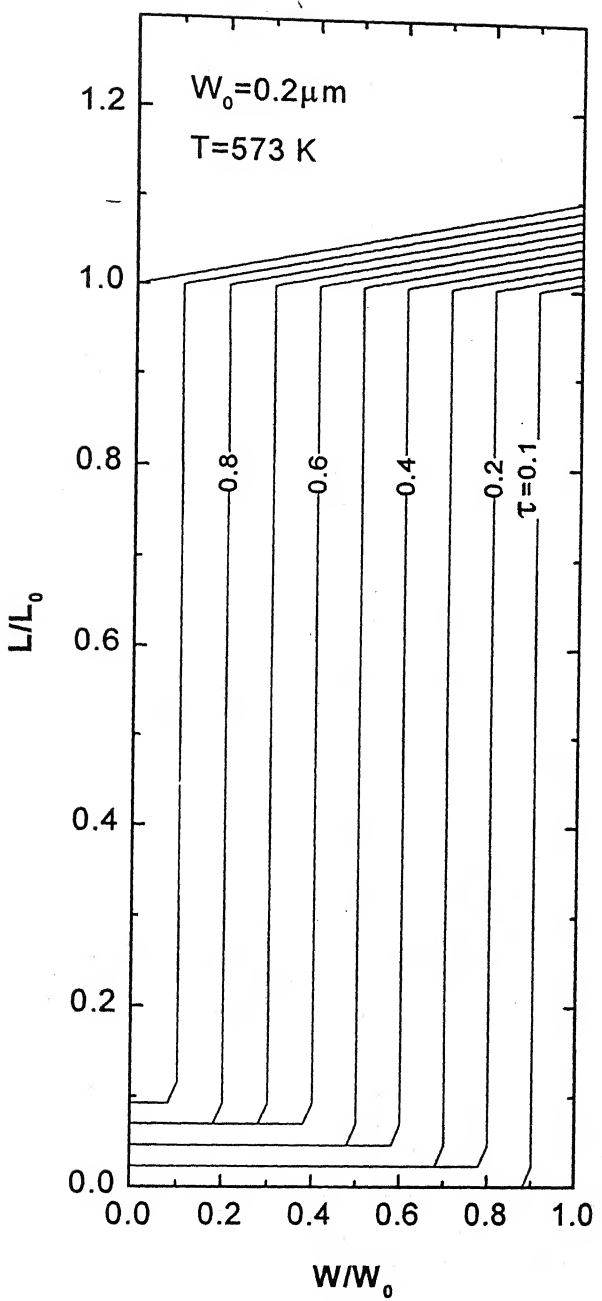


Fig.22: Isothermal deposition profile at 573 K for  $W_0 = 0.2\mu\text{m}$ ;  
total deposition time is 1207 seconds

where  $K_{\text{dielectric}}$  is the thermal conductivity of the dielectric,  $\Delta T$  is the temperature difference,  $h$  is heat transfer coefficient and  $T_s$  is the temperature of the wafer surface. For example, if we take the heat transfer coefficient as  $500\text{W/m}^2\text{K}$  (upper limit for forced convection), and surface  $T_s=298$  as  $500\text{K}$ , we find to support  $1\text{K}$  temperature difference over  $L_0$ , the dielectric should have a thermal conductivity of  $0.5\text{W/mK}$ .

The most common insulation/dielectric used in silicon technology is  $\text{SiO}_2$ . The thermal conductivity of this material in various forms ranges between  $0.6\text{-}1.5\text{ W/mK}$ [35]. Thus, the conventional ceramic is going to be just at the upper limit of required value of thermal conductivity.

As the aspect ratio of the trenches becomes more severe, polyimide films become attractive for interlayer dielectric. The polyimide materials have conductivity in range  $0.2\text{-}0.3\text{ W/mK}$ [36].

Currently, we are working with  $0.18\mu\text{m}$  design rules, metal pitch  $0.5\mu\text{m}$  and aspect ratios of trenches as 2.5. In such cases, conventional dielectric are being replaced by much lower dielectric constant materials such as Fluoropolymer films[37]. Examples in this class includes materials such as Parylene N & F, teflon, poly(naphthalene) PNT-N and poly(fluorinated naphthalene) PNT-F. Most measurements on these materials are on dielectric constant, which is lower than that of  $\text{SiO}_2$ ; less is known about their thermal conductivity. We will have to explore the thermal conductivity values for these materials, and then the application of required thermal gradient may become more convenient.

## CONCLUSION

In this work, by a two-dimensional model, we have studied in detail blanket tungsten deposition by hydrogen reduction of tungsten hexafluoride in a long rectangular trench. The effect of imposing a controlled thermal gradient, along the vertical direction of the trench is also investigated. The temperature gradient is such that, higher temperature is maintained at the base of the trench, compared to the entrance of the trench. Then these temperatures are input to the mass transport and chemical reaction model.

A sophisticated mathematical model was presented here, which deals with the diffusion and chemical reaction in a CVD reactor. The model assumes ordinary diffusion, viscous flow and Knudsen flow in a multicomponent system.

The dusty gas based flux expression[27] is used to generate a system of partial differential equations, containing variables: mole fraction of hydrogen ( $X_1$ ), mole fraction of tungsten hexafluoride ( $X_2$ ) and total pressure (P). The set of partial differential equations (PDE's) with appropriate boundary conditions is solved, using a control-volume-based finite difference method. The equations are discretized in a non-uniform grid and are solved by LU decomposition method[29]. The grid independence is verified by using 51x51 and 101x101 grids. Very little difference was found between the two results.

From the results of deposition of tungsten under isothermal condition, we find that at a lower deposition temperature (573 K), a trench 2 $\mu\text{m}$  deep and of width 0.5 $\mu\text{m}$ ,

temperatures (673 and 773 K), incomplete filling of the trench is shown, leading to the formation of a void inside the trench. At a particular deposition temperature, the size of the void increases as the trench aspect ratio increases. Moreover, for a particular aspect ratio, the void volume becomes larger with increasing temperature.

Thus it is concluded that a lower deposition temperature and a larger initial trench width promotes conformal tungsten deposition with greater step coverage. However, this prolongs the deposition time to fill a trench, which affects the throughput. Obviously, it will be much better if void free W CVD can be carried out at higher deposition temperatures.

Growth of tungsten without a void formation can be achieved by imposing a thermal gradient. This idea has never been tried before.

In our two-dimensional model, we show that the W deposition, under an imposed linear temperature gradient results in a smaller normalized void volume. For deposition at 673 K, we show that by applying a gradient of less than  $1.5 \text{ K}/\mu\text{m}$ , a trench can be completely filled, while corresponding isothermal processing lead to a void. Thus the model presented here could help the equipment designers and process engineers to establish a reliable process for blanket tungsten deposition.

Finally, in order to attain a thermal gradient of  $1.5 \text{ K}/\mu\text{m}$ , the conventional  $\text{SiO}_2$  dielectric will not be adequate. However, replacing  $\text{SiO}_2$  with polyamide and fluoropolyamide could make such thermal gradient feasible.

## REFERENCES

1. Miller, E. N. and Beinglass, I., "CVD Tungsten Interconnect and Contact Barrier Technology for VLSI", *Solid State Technology*, 1982, pp. 85-90.
2. Stefani, J. A., "Advanced Process Control of a CVD Tungsten Reactor", *IEEE Transactions in Semiconductor Manufacturing*, Vol. 9, No. 3, 1996, pp. 366-383.
3. Ireland, P.J., "High Aspect Ratio Contacts: A Review of Current Tungsten Plug Process", *Thin Solid Films*, Vol. 304, 1997, pp. 1-12.
4. Yun, J. and Park, S., "Theoretical Study of Step coverage and Comparison with Experimental Results from Low Pressure Chemical Vapor Deposition Process of Tungsten Film", *Jpn. J. Appl. Phys*, Vol. 31, 1995, pp. 3216-3226.
5. Pauleau, Y. and Lami, Ph., "Kinetics and Mechanism of Selective Tungsten Deposition by LPCVD", *J. Electrochem. Soc.*, Vol. 132, No. 11, 1995, pp. 2779-2785.
6. Broadbent, E.K. and Stacy, W.T., "Selective Tungsten Processing by Low Pressure CVD", *Solid State Technology*, 1985, pp 51-58.
7. Yeh, W., Chen, M., Wang, P., Liu, L. and Lin, M., "Selective tungsten CVD on submicron contact hole", *Thin Solid Films*, Vol. 270, 1995, pp. 462-466.
8. McConica, C.M. and Krishnamani, K., "The Kinetics of Tungsten Deposition in a Single Wafer Reactor", *J. Electrochem. Soc.: Solid State Science and Technology*, Vol 133, No. 12, 1986, pp. 2542-2548.
9. Manoj K. Jain, Timathy S. Cale, and Todd, H. Gandy, "Comparison of LPCVD Film Conformalities Predicted by Ballistic Transport-Reaction and Continuum Diffusion-Reaction Models", *J. Electrochem. Soc.*, Vol. 140, No. 1, 1993, pp. 242-247.

10. Kuijlaars, K. J., Kleijn, C. R. and Akker H.E.A., "Modeling of Selective Tungsten low-pressure CVD", *Thin Solid Films*, Vol. 290-291, 1996, pp. 406-410.
11. Werner, C., Ignacio, J., Hopfmann, C. and Patrick, F., "Equipment Simulation of Selective Tungsten Deposition", *J. Electrochem. Soc.*, Vol. 139, No. 2, 1992, pp. 566-574.
12. Bell, D.A., Falconer, J.L. and McConica, C.M., "Desorption of Tungsten Fluorides from Tungsten", *J. Electrochem. Soc.*, Vol. 142, No. 7, 1995, pp. 2401-2404.
13. Ulacia, J.I., Howell F.S., Korner, H. and Werner, Ch., "Flow And Reactor Simulation of a Tungsten CVD Reactor", *Applied Surface Science*, Vol. 38, 1989, pp. 370-385.
14. Cale, T.S., Jain M.K. and Raupp, G.B., "Programmed Rate Processing to Increase Throughput in LPCVD", *J. Electrochem. Soc.*, Vol. 137, No. 5, 1990, pp. 1526-1533.
15. Joshi, R.V., Prasad, V. and Anselmo, A., "Modeling of Growth Behavior of Low Pressure Chemical Vapor Deposition of Tungsten Films", *Thin Film Heat Transfer Properties and Processing*, HTD-Vol 184, ASME 1991.
16. Kuijlaars, K. J., Kleijn, C. R. and Akker H.E.A., "A Detailed Model for low-pressure CVD of Tungsten", *Thin Solid Films*, Vol. 270, 1995, pp. 456-461.
17. Schmitz, J. E. J. and Hasper, A., "On the Mechanism of Step Coverage of Blanket Tungsten Chemical Vapor Deposition", *J. Electrochem. Soc.*, Vol. 140, No. 7, 1993, pp. 2112-2116.
18. Chen S.H., Teng, M.C. and Liu, L.M., "W plug popping related to the W nucleation layer", *J. Vac. Sci. Technol. B* 13(3), 1995, pp. 1061-1062

19. Hasper, A., Holleman, J., Middelhoek, J., Kleijn, C. R. and Hoogendoorn, C. J., "Modeling and Optimisation of the Step Coverage of Tungsten LPCVD in Trenches and Contact Holes", "J. Electrochem. Soc., Vol. 138, No. 6, 1991, pp. 1728-1738.

20. Egashira, Y., Aita, H., Satio, T., Shimogaki, Y., Komiyama, H. and Sugawara, K., "Modeling and Simulation of Blanket Chemical Vapor Deposition of  $WSi_x$  from  $WF_6/Si_2H_6$ ", Electronics and Communication in Japan, Part 2, Vol. 79, No. 1, 1996, pp. 83-92.

21. Kleijn, C. R., Hoogendoorn, C. J., Hasper, A., Holleman, J. and Middlehoek J., "Transport Phenomena in Tungsten LPCVD in a Single-Wafer Reactor", J. Electrochem. Soc., Vol. 138, No. 2, 1991, pp. 509-517.

22. Bar, E. and Lorentz, J., "3-D Simulation of LPCDV Using Segment-Based Topography Discretization", IEEE Transactions on Semiconductor Manufacturing, Vol. 9, No. 1, February 1996, pp. 67-73.

23. Kim, B., Akiyama, Y., Imaishi, N., and Park, H., "Modeling of Tungsten Thermal Chemical Vapor Deposition", Jpn. J. Appl. Phys, Vol. 38, 1999, pp. 2881-2887.

24. Broadbent, E. K. and Ramiller C.L., "Selective Low Pressure Chemical Vapor Deposition of Tungsten", J. Electrochem. Soc.: Solid State Science and Technology, Vol. 131, No. 6, 1984, pp. 1427-1433.

25. Wolf, H., Streiter, R., Schulz, S. E. and Gessner, T., "Growth rate modeling for selective tungsten LPCVD", Applied Surface Science, Vol. 91, 1995, pp. 332-338.

26. Wang, Y. and Pollard, R., "An Approach for Modeling Surface Reaction Kinetics in Chemical Vapor Deposition Processes", J. Electrochem. Soc., Vol. 142, No. 5, 1995, pp. 1712-1725.

~~APPENDIX~~

27. Mason, E.A. and Malinquaskas, A. P., "Gas Transport in Porous Media: The Dusty Gas Model", New York, 1983

28. Deepak and Evans, J. W., "A mathematical model for chemical vapour infiltration in a microwave heated preform", J. Am. Ceramic Soc., Vol 76, No. 8, 1993, pp. 1924-1929.

29. Press, W.H., Teukolsky, S.A., Vellerling and W.T., Flannery, B.P., in Numerical Recipes in C, Second Edition, Cambridge University Press.

30. Hirshfelder, J.O., Curtiss, C.F. and Bird, R.B., in Molecular Theory of Gases and Liquids, First Edition, John Wiley and Sons. Inc.

31. Hitchman, M. L. and Jensen, K. F., in Chemical Vapor Deposition, 1993, Academic Press

32. Wolf, H. F., in Silicon Semiconductor Data, Pergamon Press, 1969 Edition.

33. Perry, J. H., in Chemical Engineering Handbook, Third edition, McGraw-Hill Book Company. Inc.

34. Reid, R.C., Prausnitz, J. M. and Sherwood, T. K., in The Properties of Gases and Liquids, Third Edition, McGraw Hill Book Company.

35. Barsoum, M., in Fundamentals of Ceramics, McGraw-Hill International Editions, 1997, pp. 505.

36. Ceramic Source, Vol. 8, 1992.

37. Homma, T., "Low dielectric constant materials and methods for interlayer dielectric films in ultralarge-scale integrated circuit multilevel interconnections", Mat. Sci. & Engg., R23, No. 6, 1998, pp. 243-285.